The 23–26 September 2012 U.K. Floods: Using PV Surgery to Quantify Sensitivity to Upper-Level Forcing

SAM HARDY,[a] DAVID M. SCHULTZ, AND GERAINT VAUGHAN

Centre for Atmospheric Science, School of Earth and Environmental Sciences, University of Manchester, Manchester, United Kingdom

ABSTRACT

Major river flooding affected the United Kingdom in late September 2012 as a slow-moving extratropical cyclone brought over 150 mm of rain to parts of northern England and north Wales. The cyclone deepened over the United Kingdom on 24–26 September as a potential vorticity (PV) anomaly approached from the northwest, elongated into a PV streamer, and wrapped around the cyclone. The strength and position of the PV anomaly is modified in the initial conditions of Weather Research and Forecasting Model simulations, using PV surgery, to examine whether different upper-level forcing, or different phasing between the PV anomaly and cyclone, could have produced an even more extreme event. These simulations reveal that quasigeostrophic (QG) forcing for ascent ahead of the anomaly contributed to the persistence of the rainfall over the United Kingdom. Moreover, weakening the anomaly resulted in lower rainfall accumulations across the United Kingdom, suggesting that the impact of the event might be proportional to the strength of the upper-level QG forcing. However, when the anomaly was strengthened, it rotated cyclonically around a large-scale trough over Iceland rather than moving eastward as in the verifying analysis, with strongly reduced accumulated rainfall across the United Kingdom. A similar evolution developed when the anomaly was moved farther away from the cyclone. Conversely, moving the anomaly nearer to the cyclone produced a similar solution to the verifying analysis, with slightly increased rainfall totals. These counterintuitive results suggest that the verifying analysis represented almost the highest-impact scenario possible for this flooding event when accounting for sensitivity to the initial position and strength of the PV anomaly.

1. Introduction

Extratropical cyclones are a major contributor to high-impact weather across the United Kingdom, with about 70% of extreme precipitation events in the United Kingdom occurring in the presence of cyclones (Pfahl and Wernli 2012) and their attendant fronts (Catto and Pfahl 2013). These heavy precipitation events can cause huge socioeconomic impacts. As a recent example, the summer and autumn floods of 2012 resulted in over GBP 1.2 billion in accumulated insured losses across the United Kingdom (Mark 2013). Although most major winter floods in the United Kingdom are connected to persistent orographically enhanced precipitation caused by atmospheric rivers (e.g., Lavers et al. 2011, 2012; Champion et al. 2015), frontal systems associated with slow-moving summer and autumn cyclones also cause U.K. precipitation extremes, with heavy rainfall often caused by slow-moving frontal rainbands to the northwest of the cyclone center (Hand et al. 2004).

The importance of upper-level precursor anomalies to cyclogenesis has long been documented, with the pioneering studies of Sutcliffe (1939, 1947), Sutcliffe and Forsdyke (1950), and Petterssen (1955) suggesting that

cyclogenesis occurred as upper-tropospheric cyclonic vorticity advection ahead of an upper-level trough moved over a surface baroclinic zone, a development pathway later classified as type-B cyclogenesis by Petterssen et al. (1962) and Petterssen and Smebye (1971). The type-B development pathway is also neatly encapsulated using the potential vorticity (PV) framework (Hoskins et al. 1985; Brennan et al. 2008), in which cyclogenesis is explained by the mutual interaction between a tropopause PV anomaly (analogous to an upper-level trough) and surface thermal anomaly (baroclinic zone). Although at first glance similar to these previous theoretical paradigms, the PV framework closes the gap between baroclinic instability (e.g., Charney 1947; Eady 1949), in which cyclogenesis results from the growth of infinitesimally small perturbations on an unstable basic state, and observations, in which a precursor upper-level anomaly is usually present prior to cyclogenesis (e.g., Uccellini 1986; Sanders 1986).

Although many cyclogenesis events involve a single upper-level precursor anomaly approaching a lower-tropospheric baroclinic zone (e.g., Uccellini et al. 1985; Reed and Albright 1986; Reed et al. 1992), some events are characterized by multiple anomalies being brought together in confluent flow and interacting prior to cyclogenesis, with lateral as well as vertical interactions between anomalies. The interaction of two upper-level anomalies may enhance baroclinicity and reduce static stability, thus preconditioning the environment for explosive cyclogenesis (Gaza and Bosart 1990). However, detailed quantitative case studies of high-impact merger events such as the March 1993 Superstorm (e.g., Huo et al. 1999a,b) and the 3 May 1999 tornado outbreak (Roebber et al. 2002) have produced counterintuitive results.

In both cases, the interaction of a northern and a southern PV anomaly was hypothesized to have caused a more extreme event. In the case of the March 1993 Superstorm, the interaction of the two PV anomalies was hypothesized to reduce static stability and enhance baroclinicity. However, when the southern anomaly was removed using PV inversion, a stronger cyclone developed because the stronger northern anomaly was able to move eastward more quickly toward the cyclone in the absence of the southern anomaly. In the 3 May 1999 tornado outbreak, the approaching southern anomaly was hypothesized to increase deep-layer shear and enhance the risk of a strong tornado outbreak, yet strengthening this anomaly using PV inversion reduced the deep-layer shear across the region, with values only marginally supportive of supercells. The strengthened southern anomaly prevented the stronger northern anomaly, with associated stronger deep-layer shear, from moving into the region,
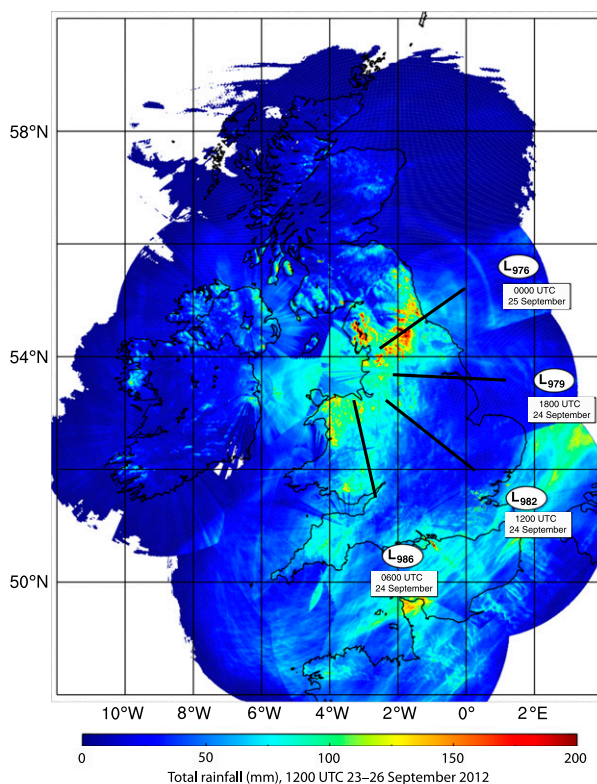

FIG. 1. The 72-h accumulated precipitation between 1200 UTC 23 Sep and 1200 UTC 26 Sep (shaded, mm) from the Met Office radar product (Met Office 2009), a 1-km horizontal grid-spacing composite CAPPI at 1-km elevation. The minimum central pressure (hPa) of the cyclone and position of the cyclone center at 6-h intervals between 0600 UTC 24 Sep and 0000 UTC 25 Sep are overlaid, alongside the orientation of the main frontal band (black lines).

thus keeping shear lower. These studies highlight the potential for lateral interactions between PV anomalies to cause seemingly counterintuitive results. Idealized modeling studies (Hakim et al. 1996; Liu and Roebber 2008) of interacting anomalies (or vortices) corroborate the low predictability of anomaly interaction by demonstrating the strong sensitivity of vortex–vortex interaction to small changes in the initial state. In such studies, latent heat release and associated PV modification (e.g., Davis et al. 1993; Stoelinga 1996) can amplify any initial perturbations applied using PV surgery, further complicating the interactions between vortices and the background flow.

A case study of a slow-moving autumn cyclone, involving interacting upper-level PV anomalies and strong latent heat release, is investigated in this paper. This storm caused major river flooding and resulted in widespread damage to homes and businesses across the United Kingdom on 23–26 September 2012, bringing over 100 mm of rain to a large swath of northern England and north Wales, with accumulations locally

exceeding 150 mm (Fig. 1). The impact of the flood was enhanced by the saturated soil conditions in northern England, resulting from the wettest summer in 100 years across England and Wales as a succession of North Atlantic depressions took a more southerly track than normal (Parry et al. 2013). The cyclone developed poleward of Tropical Cyclone Nadine in the eastern North Atlantic on 21 September 2012, as an equatorward-moving PV streamer approached Nadine from the northwest and tropical moisture was drawn poleward over a lower-tropospheric baroclinic zone (Hardy et al. 2017). The cyclone deepened further (20 hPa in 36 h) over the United Kingdom on 24–25 September as an upper-level PV anomaly approached from the west, elongating into a PV streamer and wrapping around the cyclone. A band of moderate rain ($5 \, \text{mm h}^{-1}$) developed ahead of this PV streamer to the northwest of the low center and persisted through northern England on 24–25 September as the cyclone moved through the English Channel into the North Sea. The cyclone reached its maximum intensity of 973 hPa at 0600 UTC 25 September, just off the northeast coast of England, becoming the deepest September cyclone to cross the United Kingdom in over 30 years (Met Office Press Office 2012). The intensification of the cyclone over the United Kingdom as the approaching upper-level PV anomaly elongated and wrapped around it suggests that the PV anomaly contributed to cyclogenesis.

Given the strong sensitivity of interacting anomalies in confluent flow to small perturbations (Hakim et al. 1996; Liu and Roebber 2008), this paper will examine the effect of the upper-level PV anomaly (hereafter referred to simply as the PV anomaly) approaching from the west on the development of the cyclone and resultant rainfall across the United Kingdom. Motivated by the strong impact of the flooding event, the purpose of this paper is to determine whether stronger upper-level forcing, or different phasing between the PV anomaly and cyclone, would have produced a higher-impact flooding event across the United Kingdom or whether the verifying solution represented the highest-impact event possible for this synoptic setup. The question is answered by using piecewise PV inversion to design a suite of model simulations with the strength and position of the PV anomaly modified in the initial conditions, following a similar method to previous studies by Huo et al. (1999b), Fehlmann et al. (2000), Romero (2001), and Roebber et al. (2002). Model output will be supplemented by quasigeostrophic (QG) omega equation diagnostics (e.g., Hoskins et al. 1978) to quantify the relationship between the PV anomaly and the development and maintenance of the slow-moving frontal band responsible for the flooding.
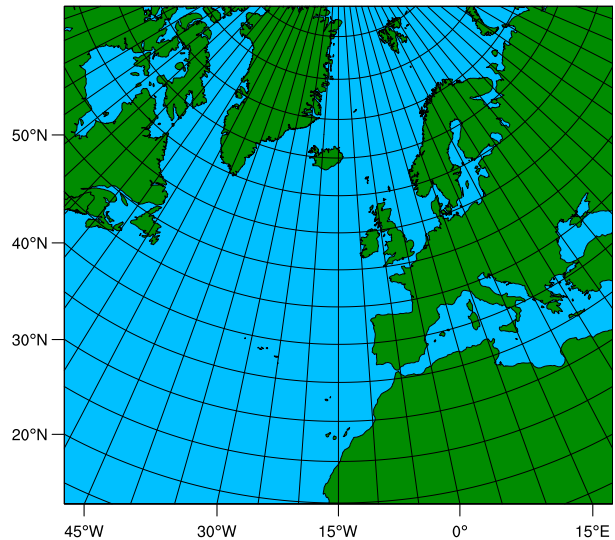

FIG. 2. Location of WRF Model domain. The horizontal grid spacing is 15 km.

The remainder of the article is structured as follows. Section 2 details the PV inversion method used to modify the initial conditions for the model sensitivity simulations and introduces the QG omega equation diagnostics. In section 3, a synoptic overview of the cyclone is presented, including analyses of the cyclone's intensification ahead of the approaching PV anomaly and the development of the slow-moving frontal rainband over the United Kingdom on 24–25 September. Section 4 then introduces the results from a control simulation of the event using the Advanced Research version of the Weather Research and Forecasting (WRF) Model, which accurately captures both the cyclone's life cycle and the distribution of the heaviest rainfall across the United Kingdom. Results from the sensitivity simulations are compared with those from the control simulation in section 5 before the relationship between upper-level forcing and the impact of the flooding event is discussed in more detail in section 6. Section 7 concludes this article.

2. Method

a. Numerical model

Version 3.5.1 of the WRF Model (Skamarock et al. 2008) was used for all simulations in this study, employing a single domain (Fig. 2) with 60 vertical levels (extending to 50 hPa), horizontal grid spacing of 15 km, and a time step of 75 s. Global Forecast System (GFS) analyses from the National Centers for Environmental Prediction (NCEP) at $0.5° \times 0.5°$ horizontal and 50-hPa vertical grid spacing (25 hPa below 750 hPa) were used as initial and lateral boundary conditions, input every 6 h. The Thompson

microphysics scheme was used (Thompson et al. 2008) with the Yonsei University planetary boundary layer scheme (Hong et al. 2006), Noah land surface model, and the fifth-generation Pennsylvania State University–National Center for Atmospheric Research Mesoscale Model (MM5) similarity surface-layer scheme, based on Monin–Obukhov theory (Monin and Obukhov 1954). Longwave and shortwave radiation were parameterized using the Rapid Radiative Transfer Model for general circulation models (RRTMG) scheme (Iacono et al. 2008), and the Kain–Fritsch scheme (Kain and Fritsch 1990, 1993; Kain 2004) was used for cumulus parameterization.

b. Potential vorticity inversion

Potential vorticity is a widely used diagnostic in synoptic meteorology because it encapsulates the information essential to extratropical cyclogenesis in a single variable, which is conserved for adiabatic, frictionless flow (Rossby 1940; Ertel 1942):

$$q = \frac{1}{\rho} \boldsymbol{\eta} \cdot \nabla \theta, \tag{1}$$

where q is the PV, ρ is the density, $\boldsymbol{\eta}$ is the absolute vorticity vector, and $\nabla \theta$ is the three-dimensional gradient of the potential temperature θ. Moreover, its invertibility principle (e.g., Hoskins et al. 1985) allows one to deduce dynamically relevant meteorological fields (wind, height, temperature, and stability) associated with individual PV anomalies, given the boundary distribution of θ and a suitable balance condition relating the wind and geopotential height fields, as demonstrated by Davis and Emanuel (1991). This method of piecewise PV inversion provides a powerful and dynamically consistent way of quantifying the influence of individual PV anomalies on extratropical cyclogenesis, such as the vertical interactions between diabatically generated lower-tropospheric PV anomalies and tropopause PV anomalies (e.g., Stoelinga 1996; Ahmadi-Givi et al. 2004) or the lateral interactions between upper-tropospheric PV anomalies (e.g., Hakim et al. 1996; Huo et al. 1999a).

Furthermore, PV inversion has been used to design experiments in which individual PV anomalies are removed from, or added to, the model initial state and the model rerun to quantify the importance of the anomaly to the evolution of the downstream flow. This technique has been applied extensively in studies of extratropical cyclones (e.g., Huo et al. 1999b; Romero 2001; Roebber et al. 2002) and of tropical cyclones undergoing extratropical transition (e.g., McTaggart-Cowan et al. 2001, 2004; Agustí-Panareda et al. 2004; Riemer et al. 2008; Grams et al. 2011). In this study, the PV anomaly responsible for the deepening of the cyclone over the United Kingdom and the associated rainfall is isolated

using this technique, known as PV "surgery." The PV surgery method applies the piecewise PV inversion technique of Davis and Emanuel (1991) to isolate the selected anomaly and to calculate its balanced wind, height, and temperature fields. The balanced flow associated with the anomaly is then added to or subtracted from the initial conditions to obtain a modified initial state before the model is rerun.

In this study, PV surgery is performed on the GFS 0.5° analyses before they are input into WRF. To isolate the PV anomaly, the mean state is subtracted from the instantaneous field (Fig. 3a) to give the anomalous PV (Fig. 3b) at 0600 UTC 23 September. The mean state is calculated by temporally averaging the GFS 0.5° analyses at 6-h intervals between 0600 UTC 20 September and 0600 UTC 26 September, creating a 6-day mean centered about 0600 UTC 23 September, following a similar method to previous studies isolating upper-tropospheric PV anomalies (e.g., Davis 1992; Stoelinga 1996; McTaggart-Cowan et al. 2001). The wind, height, and temperature perturbations associated with the isolated anomaly (Fig. 4) are calculated using the piecewise PV inversion technique of Davis and Emanuel (1991) under the assumption of Charney (1955) nonlinear balance. The anomaly is defined as the region of perturbation PV ≥ 0.4 potential vorticity units (PVU; 1 PVU $= 10^{-6} \, \mathrm{K \, kg^{-1} \, m^2 \, s^{-1}}$) bounded by the grid box shown (Figs. 3 and 5a), between 50 and 600 hPa. Any regions of negative perturbation PV were set to a small, positive value to avoid numerical problems with the inversion scheme. The inversion was performed on a 361×131 grid with 0.5° (about 55 km) horizontal grid spacing (approximately $19\,855 \, \mathrm{km} \times 7205 \, \mathrm{km}$) centered over the eastern North Atlantic. Homogeneous Dirichlet conditions were applied on the lateral boundaries, with Neumann conditions applied on the top and bottom boundaries. The lower boundary of the inversion domain was restricted to 850 hPa to avoid numerical errors in the boundary layer associated with unstable lapse rates (e.g., Ahmadi-Givi et al. 2004; Bracegirdle and Gray 2009), with the upper boundary at 20 hPa. This method was used to design a suite of simulations in which the strength of the PV anomaly and its position relative to the cyclone were modified in the initial conditions, before the model was rerun (summarized in Table 1). The results of these simulations will be discussed further in sections 5 and 6.

c. Quasigeostrophic omega equation diagnostics

To quantify the large-scale vertical motion associated with the PV streamer and its contribution to the maintenance of the rainfall band responsible for the flooding, the right-hand side of the **Q**-vector form of the QG omega equation (Hoskins et al. 1978; Hoskins and
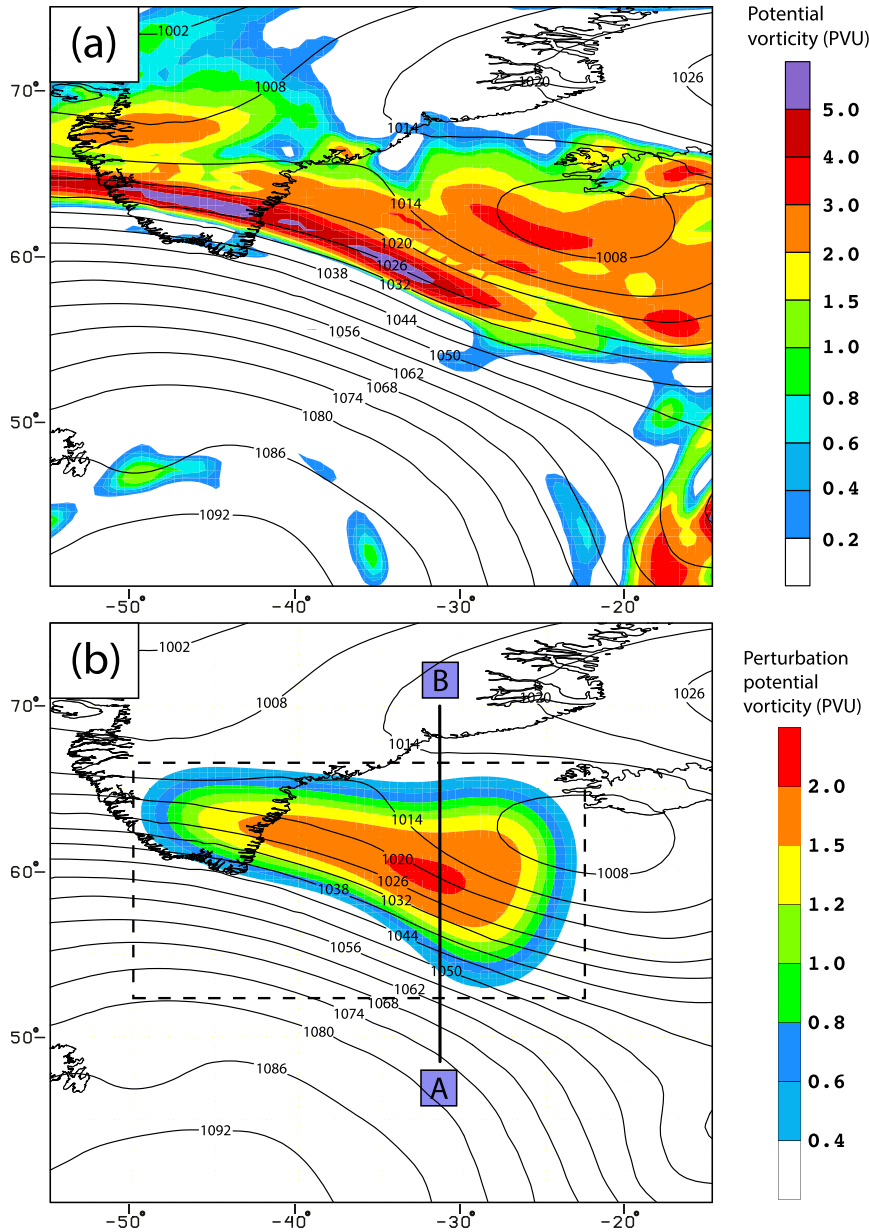
FIG. 3. (a) Full 250-hPa PV (shaded, PVU) at 0600 UTC 23 Sep. (b) 250-hPa perturbation PV (shaded, PVU) at 0600 UTC 23 Sep, calculated by subtracting the 6-day mean from the instantaneous PV field (a) using the PV inversion method described in section 2. Overlaid is 250-hPa geopotential height (black contours, dam). The box in (b) (black dashed lines) bounds the region enclosing the anomaly, and the transect A–B corresponds to the vertical cross-sectional location in Fig. 4. In (b), the perturbation field was smoothed using three passes from a 25-point smoother applied over the entirety of the domain.

Pedder 1980) is evaluated at 700 hPa, minus the beta term, following Bluestein (1992, p. 353):

$$\left(\nabla_p^2 + \frac{f_0^2}{\sigma}\frac{\partial^2}{\partial p^2}\right)\omega = -2\nabla_p \cdot \mathbf{Q}, \qquad (2)$$

where $\mathbf{Q}$ is defined following Bluestein (1992, p. 352) as

$$\mathbf{Q} = -\frac{R}{\sigma p}\begin{pmatrix} \dfrac{\partial \mathbf{V}_g}{\partial x}\cdot \nabla_p T \\[2ex] \dfrac{\partial \mathbf{V}_g}{\partial y}\cdot \nabla_p T \end{pmatrix} = \begin{pmatrix} Q_1 \\ Q_2 \end{pmatrix}. \qquad (3)$$

Regions of $\mathbf{Q}$-vector convergence $(-2\nabla_p \cdot \mathbf{Q} > 0)$ are associated with QG forcing for ascent, with regions of
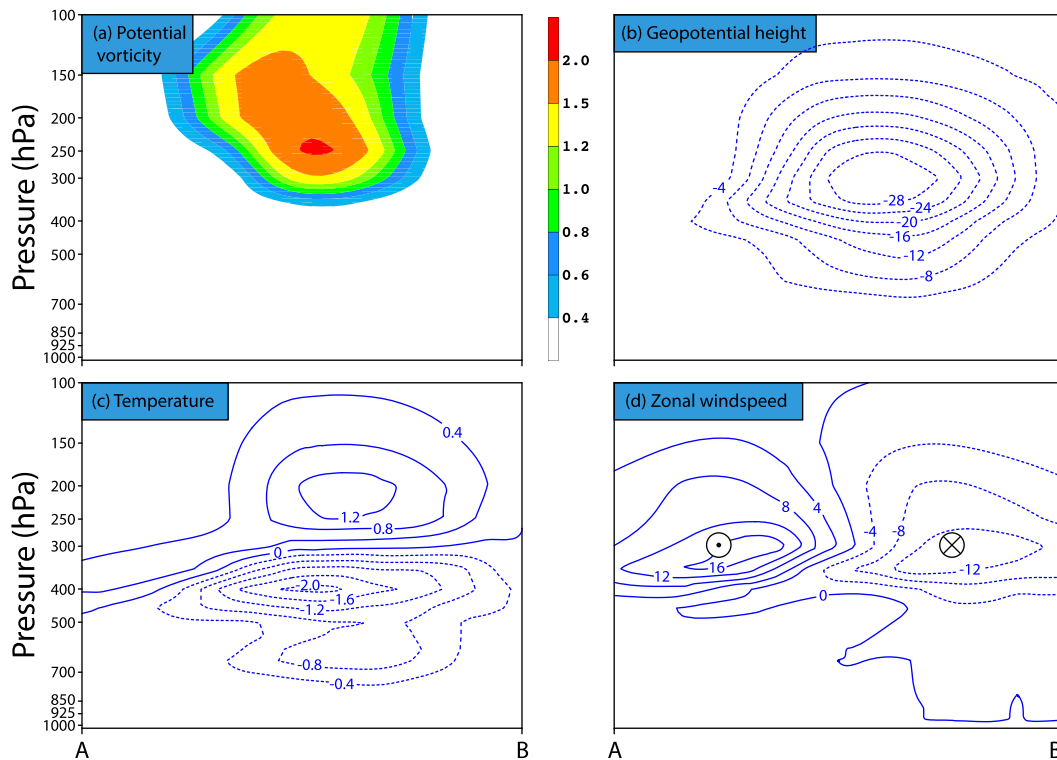
FIG. 4. North–south vertical cross sections along the line A–B in Fig. 3b. (a) Perturbation PV (shaded, PVU), (b) balanced geopotential height (m), (c) temperature (K), and (d) zonal wind speed (m s^{-1}) associated with the inverted PV anomaly in (a). In (b)–(d), negative values are dashed, and positive values are solid. In (d), flow is westerly (out of the page) to the south of the anomaly and easterly (into the page) north of the anomaly.

Q-vector divergence ($-2\nabla_p \cdot \mathbf{Q} < 0$) likewise associated with forcing for descent, from Eq. (2). Although Eq. (2) is likely to underestimate the magnitude of vertical motion in regions of strong latent heat release, the equation accurately captures the spatial variability of the vertical motion field on the synoptic scale (e.g., Quinting and Jones 2016), making it suitable for use in this study. The General Meteorology Package (GEMPAK), version 7.2, was used to compute the right-hand side of Eq. (2) from the 15-km simulation output data; smoothing was applied to the 15-km data to filter out features with a grid spacing of 200 km or less [Battalio and Dyer (2017) and references therein]. The results from these calculations are discussed in more detail in sections 4–6.

3. Synoptic overview

The synoptic evolution of this event is documented using the GFS 0.5° analyses previously described in section 2, complemented with the Met Office radar product (Met Office 2009), a 1-km horizontal grid-spacing composite constant-altitude plan position indicator (CAPPI) at 1-km elevation.

a. Cyclone interaction with upper-level PV anomaly

At 0600 UTC 23 September, the cyclone was situated to the northwest of Spain with a central pressure of 992 hPa (Fig. 5a), having earlier developed on 21 September within a plume of tropical moisture along a lower-tropospheric baroclinic zone poleward of Tropical Cyclone Nadine[1] (Hardy et al. 2017). Poleward and upstream of the cyclone, a region of high-PV air (≥4 PVU) on the 325-K isentropic surface was situated over Iceland and Greenland, associated with a slow-moving trough (Fig. 5a). The cyclone maintained its central pressure as it moved slowly northeast between 0600 and 1800 UTC 23 September before starting to deepen from 1800 UTC 23 September as a PV anomaly on the leading edge of an elongated band of high-PV air (≥8 PVU on 325 K) moved southeastward around the southern flank of the high-PV reservoir over Iceland and Greenland (Figs. 5b,c). The approaching PV anomaly elongated as it approached the cyclone between 1800 UTC 23 September and 0600 UTC 24 September, wrapping around the

---

[1] Nadine is located farther south at around 30°N and out of the domain shown.

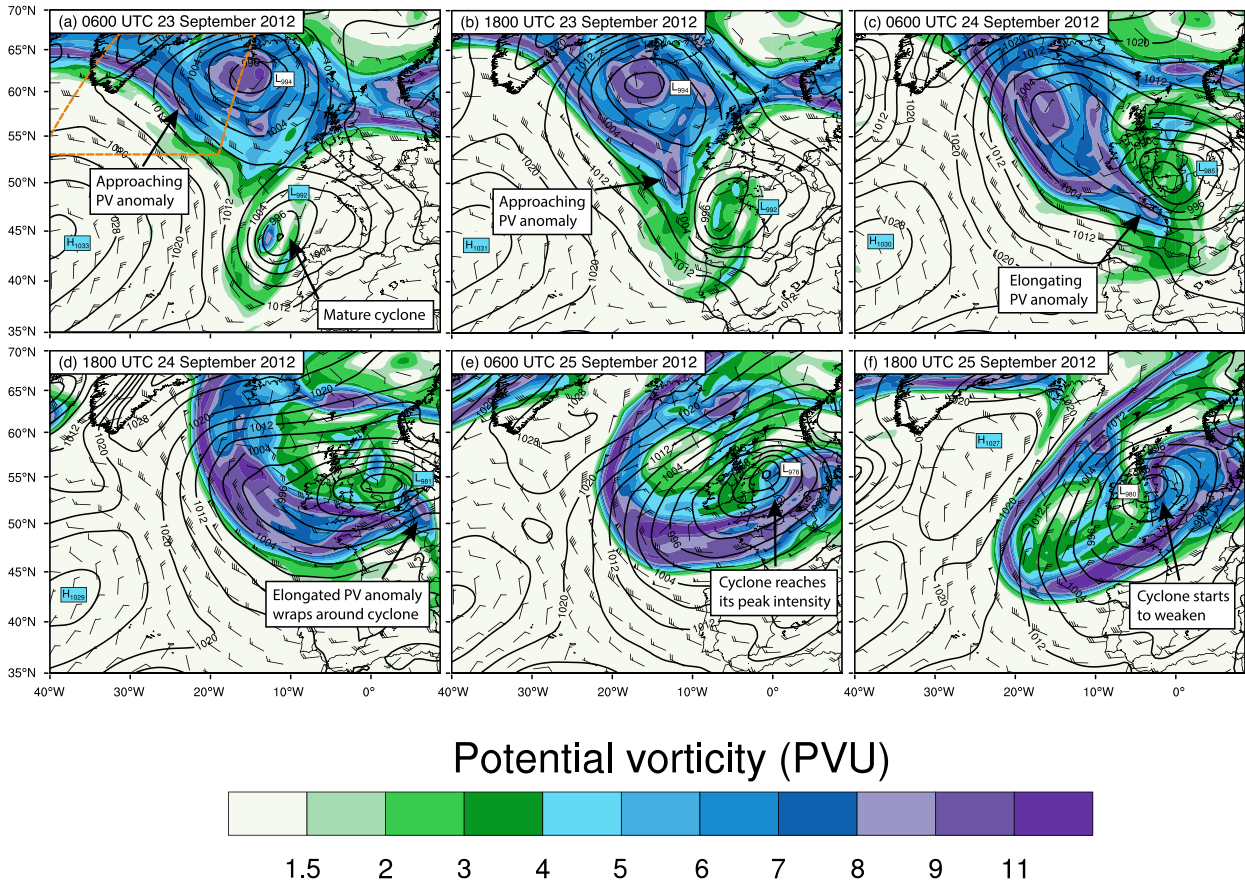FIG. 5. PV (shaded, PVU) and horizontal winds (half-barb represents 2.5 m s^{-1}; full barb represents 5 m s^{-1}; pennant represents 25 m s^{-1}) on the 325-K isentropic surface, and mean sea level pressure (black contours, hPa), from GFS 0.5° analysis data. (a) 0600 UTC 23 Sep, (b) 1800 UTC 23 Sep, (c) 0600 UTC 24 Sep, (d) 1800 UTC 24 Sep, (e) 0600 UTC 25 Sep, and (f) 1800 UTC 25 Sep. In (a), the box (orange dashed line) bounds the region enclosing the PV anomaly for the PV inversions and corresponds to the box in Fig. 3.

cyclone as the cyclone moved over the United Kingdom and continued to deepen on 24 September (Figs. 5c,d). Observations suggested that the deepening cyclone reached its maximum intensity of 973 hPa at 0600 UTC 25 September (Met Office Press Office 2012), with GFS 0.5° analysis capturing a slightly shallower cyclone (976 hPa) just off the northeast coast of England (Fig. 5e), before moving back westward and slowly weakening as the stratospheric air (≥8 PVU) on 325 K moved directly over the cyclone center (Fig. 5f).

b. Rainfall over the United Kingdom

As the cyclone approached the United Kingdom from the southwest between 1800 UTC 23 September and 0600 UTC 24 September, warm sector air with total precipitable water >25 mm moved north across much of central and southern England behind the warm front, the latter identifiable as the zonally oriented band of 800–925-hPa PV > 1.5 PVU stretching across north Wales and central England at 1800 UTC 23 September

(Fig. 6a). As the upper-level PV anomaly approached from the west and the cyclone deepened, a second region of diabatically generated PV > 1.5 PVU developed northwest of the low center in conjunction with a maximum in lower-tropospheric Petterssen (1936) frontogenesis (Fig. 6b). Rain turned heavy and persistent in this region of enhanced frontogenesis and cyclonic PV northwest of the low center, with rainfall rates locally peaking above 15 mm h^{-1} across Wales and southern England (Fig. 7a).

As the cyclone center moved northeastward and the tongue of total precipitable water >25 mm associated with the warm sector narrowed (Fig. 6c), the frontal band pivoted around the low center to become more zonally oriented (Figs. 7b,c), with rainfall continuing through much of northern England as a result. The pivoting motion of the frontal band [oriented northwest–southeast at 0600 UTC 24 September (Fig. 6b), west-northwest–east-southeast at 1800 UTC 24 September (Fig. 6c), and southwest–northeast by 0600 UTC 25 September

TABLE 1. Summary and description of WRF control and sensitivity simulations, all initialized at 0600 UTC 23 Sep.

Simulation	Description	Central pressure at 0600 UTC 25 Sep (hPa)	Area-averaged total precipitation (mm) between 1200 UTC 23 Sep and 1200 UTC 26 Sep and percentage difference with CNTRL (percent)
NOPV	PV anomaly removed	982	32.39 (−11.7)
0.5*PV	PV anomaly weakened by 50%	982	33.51 (−8.7)
0.75*PV	PV anomaly weakened by 25%	974	36.50 (−0.5)
CNTRL	Control simulation	972	36.69
1.25*PV	PV anomaly strengthened by 25%	977	33.41 (−8.9)
1.5*PV	PV anomaly strengthened by 50%	980	31.61 (−13.8)
2*PV	PV anomaly doubled in strength	983	29.14 (−20.6)
PVF_500	PV anomaly moved 500 km farther from the cyclone	979	31.53 (−14.1)
PVF_250	PV anomaly moved 250 km farther from the cyclone	981	29.96 (−18.3)
PVN_250	PV anomaly moved 250 km closer to the cyclone	968	38.80 (+5.8)
PVN_500	PV anomaly moved 500 km closer to the cyclone	969	36.19 (−1.4)

(Fig. 6d)] resulted in several locations in northern England recording over 40 h of continuous precipitation between 24 and 26 September (not shown). Particularly high precipitation totals were recorded along windward eastern slopes of the Pennines in North Yorkshire with over 150 mm falling onto sloping terrain (Fig. 1), resulting in widespread flooding in the flood-prone city of York. The control simulation, discussed further in section 4, accurately captured this maximum in rainfall duration over the eastern slopes of the Pennines (Fig. 7d).

4. Control simulation

The control simulation (CNTRL), initialized at 0600 UTC 23 September, accurately resolved the synoptic-scale evolution of the cyclone, capturing its moderate deepening between 1800 UTC 23 September and 0600 UTC 25 September (Fig. 8) as the approaching PV anomaly elongated into a PV streamer and wrapped around the cyclone. The path of the simulated cyclone through the English Channel and into the North Sea on 24–25 September compares favorably with the analyzed path based on Met Office surface charts (Fig. 9), and the simulation also accurately captured the timing of maximum cyclone intensity (972 hPa vs the observed value of 973 hPa) at 0600 UTC 25 September just off the northeast coast of England.

As the cyclone approached the United Kingdom from the southwest on 24 September, an initially broad, zonally oriented region of light precipitation (rainfall rates generally between 1 and 2 mm h^{-1}) associated with the warm front (Fig. 10a) thinned and fragmented (Figs. 10c,e) as the cyclone moved northeastward. All the while, another band of fragmented rainfall to the immediate west of the low center (Fig. 10a) organized into a more persistent band stretching northwest to southeast across south Wales and southwest England at 0600 UTC 24 September (Fig. 10c), slowly pivoting cyclonically (Fig. 10e). The orientation of the simulated band at 0600 UTC 24 September compares favorably with observations from the Met Office CAPPI at 1-km elevation (cf. Fig. 7a and Fig. 10c), although the 15-km simulation with parameterized convective precipitation underestimated the observed peaks in the rainfall rates (simulated maxima close to 8 mm h^{-1} compared to observed values closer to 15 mm h^{-1}). The frontal band developed in a region of persistent QG forcing for ascent ahead of the elongating upper-tropospheric PV streamer, with **Q**-vector convergence on the warm side of the front suggestive of a weakly frontogenetic environment between 0000 and 1200 UTC 24 September (Figs. 10b,d,f).

As the cyclone deepened between 1800 UTC 24 September and 0600 UTC 25 September and the frontal band pivoted cyclonically with the low center, moderate rainfall continued over northern England (Figs. 11a,c,e). The pivoting rainfall band was consistent with a narrowing of the warm sector and a consequent thinning of the thermal ridge at 700 hPa, characterized by the region of $\theta > 302$ K over eastern England and the North Sea (Figs. 11b,d,f). The rainfall band was maintained in a region of 700-hPa **Q**-vector convergence and associated QG forcing for ascent (1–2 × 10^{-17} m kg^{-1} s^{-1}) ahead of the PV streamer (Figs. 11b,d,f) throughout the band's evolution on 24–25 September. Furthermore, the back edge of the rainfall band was collocated with the region of 700-hPa QG forcing for descent behind the PV streamer throughout the band's evolution (Figs. 10 and 11), consistent with the hypothesis that large-scale vertical motion patterns associated with the PV streamer contributed to the maintenance of the band.
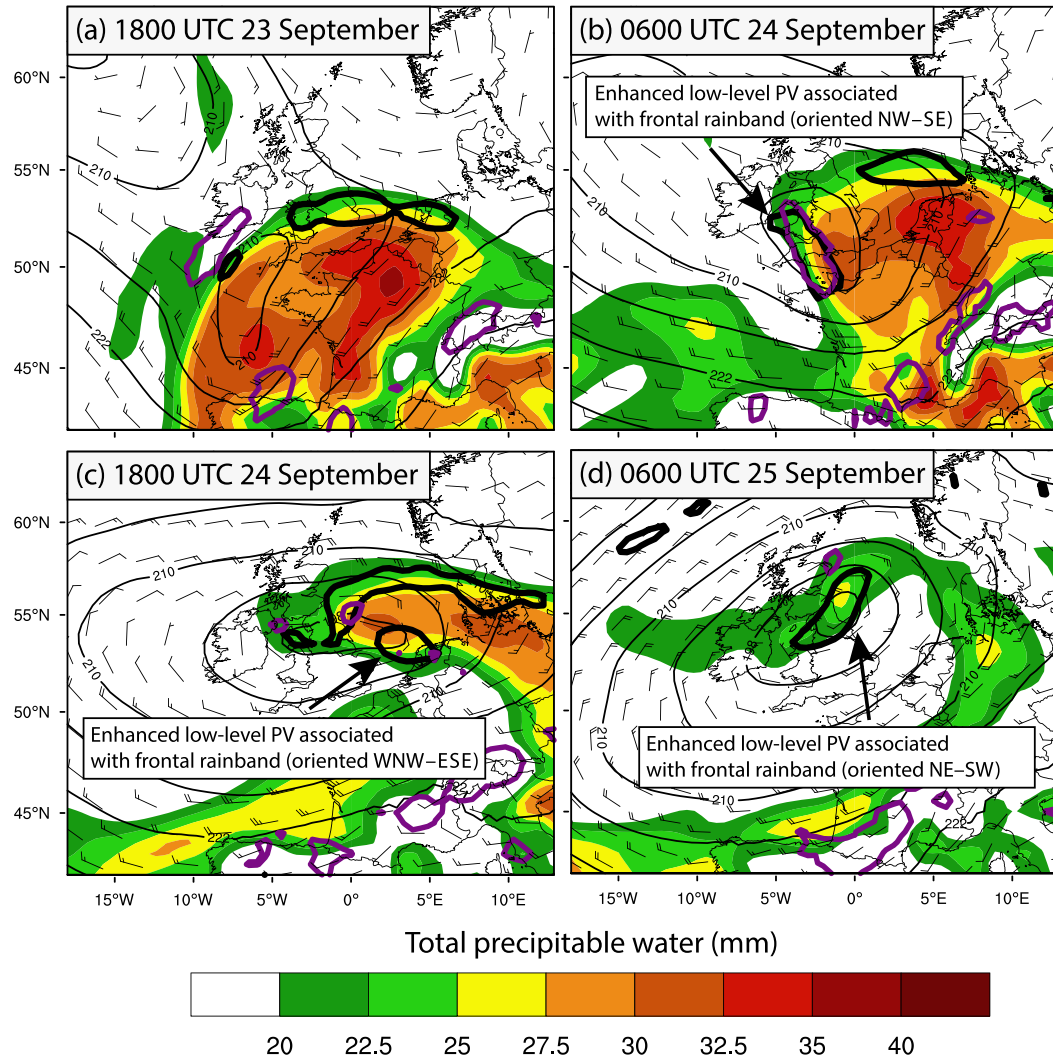
FIG. 6. Total precipitable water (shaded, mm), 850-hPa geopotential height (thin black contours, dam), and 700–850-hPa layer-averaged horizontal winds (half-barb represents $2.5\,\mathrm{m\,s^{-1}}$; full barb represents $5\,\mathrm{m\,s^{-1}}$; pennant represents $25\,\mathrm{m\,s^{-1}}$) from GFS 0.5° analysis data. Overlaid are PV greater than 1.5 PVU (black contour) and Petterssen frontogenesis greater than $0.8\,\mathrm{K\,(100\,km)^{-1}\,(3\,h)^{-1}}$ averaged over the 800–925-hPa layer. (a) 1800 UTC 23 Sep, (b) 0600 UTC 24 Sep, (c) 1800 UTC 24 Sep, and (d) 0600 UTC 25 Sep.

The control simulation (CNTRL) accurately simulated the track of the low center (Fig. 9), its moderate deepening between 1800 UTC 23 September and 0600 UTC 25 September (20 hPa in 36 h) and the pivoting of the main rainfall band (Figs. 10 and 11) and the maximum in accumulated precipitation in northeast England (Fig. 9). However, rainfall accumulations were smaller than observations because of the failure of the model to simulate the enhancement of the rainfall rates over the highest topography in northern England (cf. Fig. 7 and Fig. 9) and the heaviest rain within the band (cf. Fig. 7a and Fig. 10c). Additionally, although the swath of the largest rainfall accumulations in northern England and Wales was

adequately simulated in CNTRL, accumulations in southwest England were much lower than suggested by observations. Despite these differences, for the purposes of this study, CNTRL is accurate enough, allowing us to confidently proceed with sensitivity simulations.

5. Sensitivity simulations

The importance of upper-level forcing associated with the approaching PV anomaly to the intensification of the cyclone and the persistence of the frontal band responsible for the flooding is investigated in a series of WRF simulations with modified initial conditions,
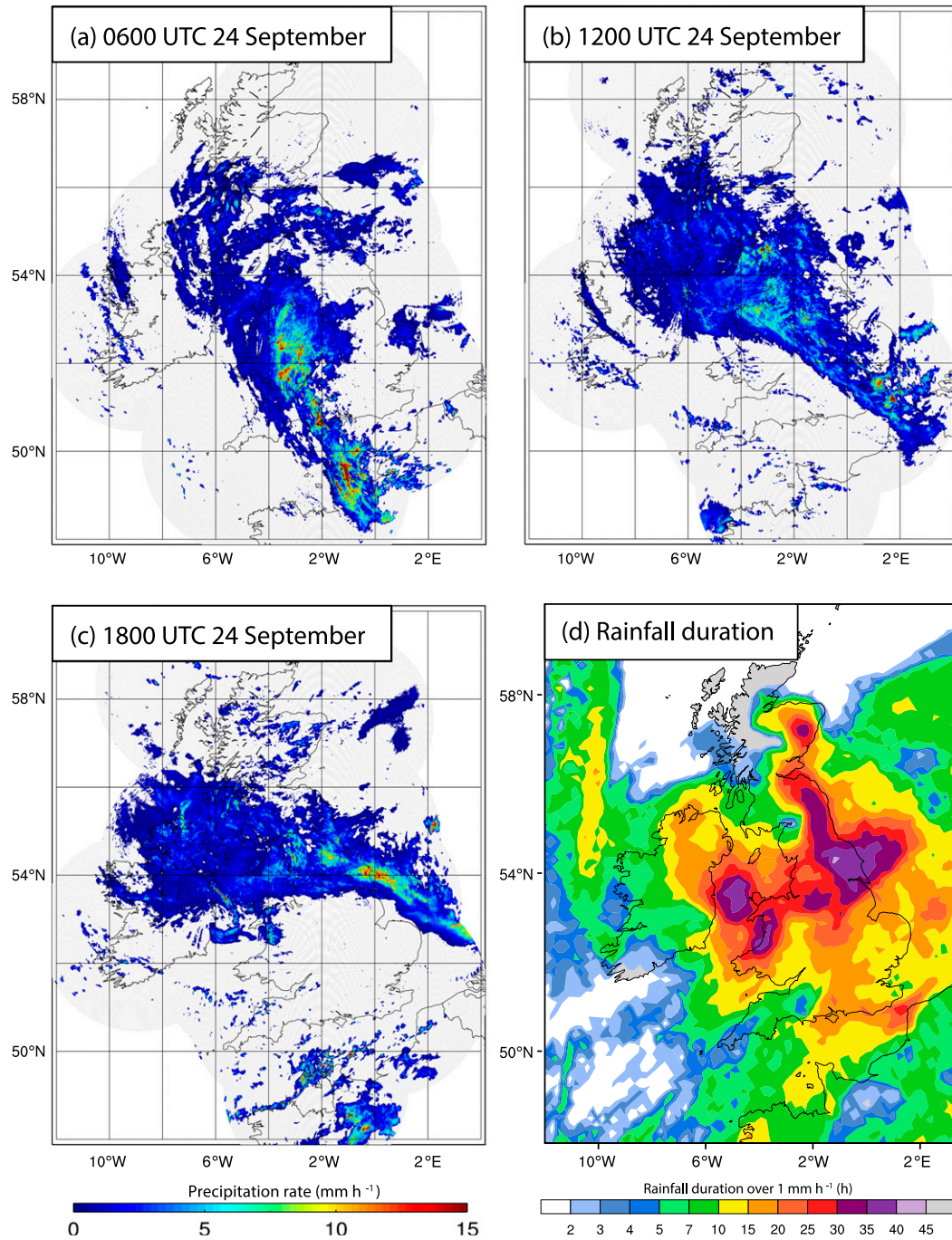
FIG. 7. Precipitation rate (shaded, mm h^{-1}) from the Met Office 1-km grid-spacing composite CAPPI at 1-km elevation (Met Office 2009) showing the location of the main frontal band associated with the cyclone: (a) 0600 UTC 24 Sep, (b) 1200 UTC 24 Sep, and (c) 1800 UTC 24 Sep. (d) Rainfall duration ($\geq$1 mm h^{-1}) from the WRF control simulation, calculated between 1200 UTC 23 Sep and 1200 UTC 26 Sep.
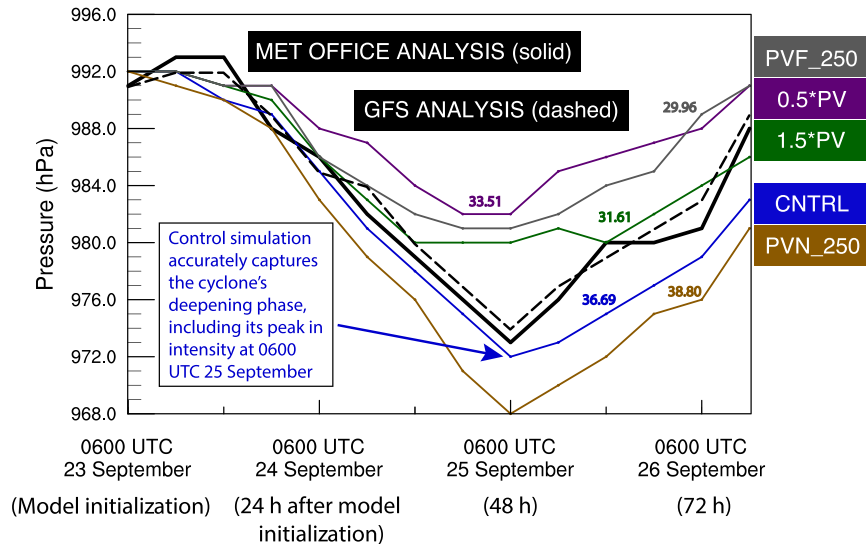
FIG. 8. Time series of mean sea level pressure for the WRF control simulation (CNTRL) and Met Office and GFS 0.5° analysis data at 6-h intervals between 0600 UTC 23 Sep and 1200 UTC 26 Sep. Also shown are sensitivity simulations with the approaching PV anomaly weakened by 50% (0.5*PV) and strengthened (1.5*PV) by 50%, and simulations with the anomaly moved 250 km farther away from the cyclone (PVF_250) and 250 km nearer to the cyclone (PVN_250) at model initialization (0600 UTC 23 Sep).

summarized in Table 1. In these simulations, the strength of the PV anomaly and its position relative to the cyclone are altered using PV surgery (see section 2). Given the inherent uncertainty associated with interacting PV anomalies (e.g., Hakim et al. 1996; Liu and Roebber 2008), our method applies a range of perturbations to the initial state rather than simply removing the anomaly or doubling its strength as was done in previous sensitivity studies (e.g., Huo et al. 1999b; Romero 2001).

a. PV anomaly strength

Six simulations were run in which the strength of the PV anomaly was altered, with three simulations strengthening the anomaly by 25% (1.25*PV), 50% (1.5*PV) and 100% (2*PV) and three corresponding simulations weakening the anomaly by the same amounts (0.75*PV, 0.5*PV, and NOPV). The results from all simulations are summarized in Fig. 12, which documents the relationship between cyclone intensity and accumulated rainfall as the strength of the upper-level anomaly is modified. Weakening the PV anomaly (0.75*PV, 0.5*PV, and NOPV) resulted in a shallower cyclone with lower accumulated rainfall totals across the United Kingdom (Fig. 12), in line with conventional ideas of height falls and QG ascent ahead of an upper-level anomaly contributing to cyclogenesis and precipitation (e.g., Petterssen and Smebye 1971; Hoskins et al. 1985).

Somewhat counterintuitively, however, increasing the strength of the PV anomaly by 25% (1.25*PV), 50% (1.5*PV), and 100% (2*PV) also resulted in progressively weaker cyclones (5, 8, and 11 hPa shallower than CNTRL, respectively) with lower accumulated rainfall totals (8.9%, 13.8%, and 20.6% reductions relative to CNTRL, respectively) across the United Kingdom (Fig. 12). Indeed, the strongest anomaly (2*PV) produced the lowest accumulated rainfall total (reduced by 20.6% relative to CNTRL), and the shallowest cyclone (minimum central pressure 11 hPa higher than in CNTRL). Strengthening the PV anomaly also brought about a poleward shift in the region of largest accumulations (discussed further in section 6). This poleward shift would have further reduced the impact of the rainfall event over the United Kingdom, given that the event's impact was enhanced by the antecedent conditions across England and Wales (leading to saturated soil conditions across northern England) and that rainfall totals between April and July 2012 were lower over Scotland than across much of England and Wales, which had experienced its wettest summer in 100 years (Parry et al. 2013).

b. PV anomaly positioning

The positioning of a PV anomaly relative to a downstream cyclonic disturbance (such as an extratropical cyclone, tropical cyclone, or diabatic Rossby wave) can modify the subsequent behavior of the disturbance
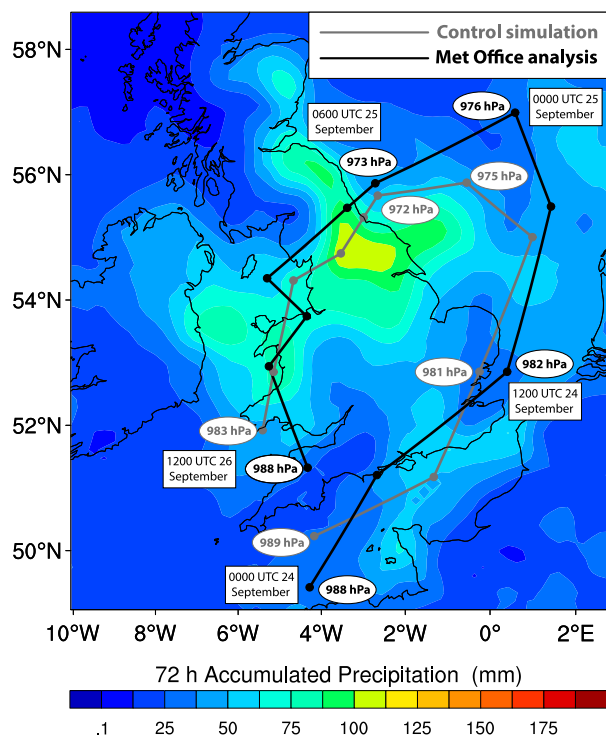
FIG. 9. The 72-h accumulated precipitation between 1200 UTC 23 Sep and 1200 UTC 26 Sep from the WRF Model control simulation (CNTRL). Overlaid are the positions of the cyclone center and the minimum central pressure of the cyclone at 6-h intervals from CNTRL (gray) and Met Office analysis (black) between 0000 UTC 24 Sep and 1200 UTC 26 Sep.

when the PV anomaly approaches, as shown in previous studies on tropical cyclones undergoing extratropical transition (e.g., Klein et al. 2002; Ritchie and Elsberry 2007; Riemer and Jones 2010; Grams et al. 2013), on diabatic Rossby waves (e.g., Boettcher and Wernli 2011), and on the interaction between Nadine and the PV streamer (Pantillon et al. 2016). As such, four further simulations were run (Table 1) in which the spatial location of the PV anomaly was modified in the initial conditions, with the anomaly moved 250 and 500 km nearer to the cyclone (southeast) in two simulations (PVN_250 and PVN_500, respectively) and likewise moved 250 and 500 km farther from the cyclone (northwest) in two additional simulations (PVF_250 and PVF_500, respectively).

Whereas the results in the previous subsection indicate that the observed rainfall accumulations and cyclone intensity represent an upper limit on the impact of this flooding event, moving the anomaly closer to the cyclone (PVN_250 and PVN_500) at model initialization produced a deeper cyclone, though not necessarily more rainfall. However, the 5.8% increase in accumulated precipitation in PVN_250 relative to CNTRL (Fig. 13) is much smaller than the biggest decreases in

precipitation from the other sensitivity simulations (18.3% in PVF_250 and 20.6% in 2*PV). The implication is that although deeper cyclones developed in PVN_250 and in PVN_500 than in CNTRL, by 4 and 3 hPa, respectively, the verifying solution and that in CNTRL represent almost the highest-impact scenario possible (as measured by the accumulated rainfall and cyclone intensity) after accounting for sensitivity to the initial position and strength of the PV anomaly.

6. Discussion

The control and sensitivity simulations can be subjectively grouped into two main scenarios based on the intensity and persistence of the rainfall. In the first and verifying scenario, the elongating PV streamer wrapped around the deepening cyclone, and QG forcing for ascent ahead of the slow-moving PV streamer helped maintain an environment favorable for precipitation along the pivoting frontal band across northern England (representative simulations were CNTRL, 0.75*PV, PVN_250, and PVN_500). These high-impact solutions are characterized by the largest accumulated rainfall totals (Figs. 12 and 13). In the second scenario (1.25*PV, 1.5*PV, 2*PV, PVF_250, and PVF_500), the PV anomaly remained compact instead of elongating into a streamer and moved quickly poleward over Ireland instead of eastward over the United Kingdom, resulting in smaller rainfall accumulations (Figs. 12 and 13), and the rainfall maximum shifted about 350 km north into Scotland. In the two remaining simulations, 0.5*PV and NOPV, the upper-level PV evolved similarly as in the high-impact solutions, but rainfall rates were much lower than in the other simulations.

a. Differences in upper-level PV

The differences in the evolution of 325-K PV between the high-impact (CNTRL), compact-anomaly (1.5*PV), and weak (0.5*PV) solutions are illustrated in more detail in Figs. 14 and 15. The evolution in 1.5*PV contrasts strongly with that in CNTRL, with the more compact trough moving poleward over Ireland (Figs. 14a,b) and rotating cyclonically westward (Figs. 15a,b) rather than elongating and wrapping around the cyclone as in CNTRL (Figs. 14c,d and 15c,d). In 0.5*PV, the PV anomaly elongated as in CNTRL (Figs. 14e,f) but did not then wrap around the surface cyclone to the same extent, remaining oblate (Figs. 15c–f). The surface cyclone took a similar track to that in CNTRL (Figs. 15c–f) but deepened more slowly ahead of the weaker anomaly (Fig. 8). The slower deepening of the cyclone ahead of the weaker PV anomaly in 0.5*PV is consistent with type-B cyclogenesis (e.g., Petterssen
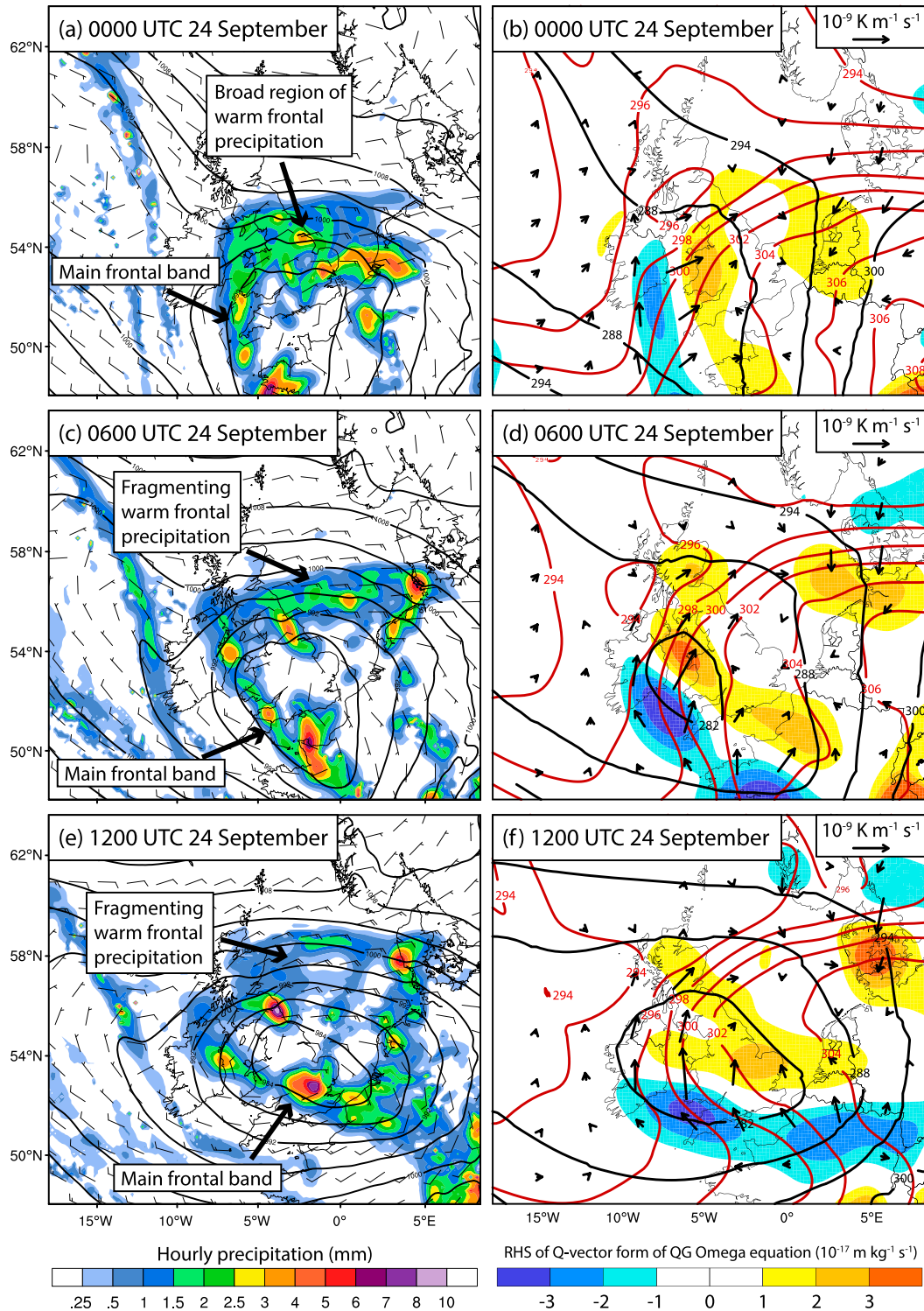
FIG. 10. (a),(c),(e) Hourly accumulated precipitation (shaded, mm), 10-m winds (half-barb represents 2.5 m s^{-1}; full barb represents 5 m s^{-1}; pennant represents 25 m s^{-1}), and mean sea level pressure (black contours, hPa). (b),(d),(f) Right-hand side of the **Q**-vector form of the QG omega equation (shaded, 10^{-17} m kg^{-1} s^{-1}), with warm colors denoting forcing for ascent and cold colors denoting forcing for descent, **Q** vectors (arrows in 10^{-9} K m^{-1} s^{-1}), geopotential height (black contours, dam), and potential temperature (red contours, K) at 700 hPa. Results shown are from CNTRL and are valid at (a),(b) 0000 UTC 24 Sep; (c),(d) 0600 UTC 24 Sep; and (e),(f) 1200 UTC 24 Sep.
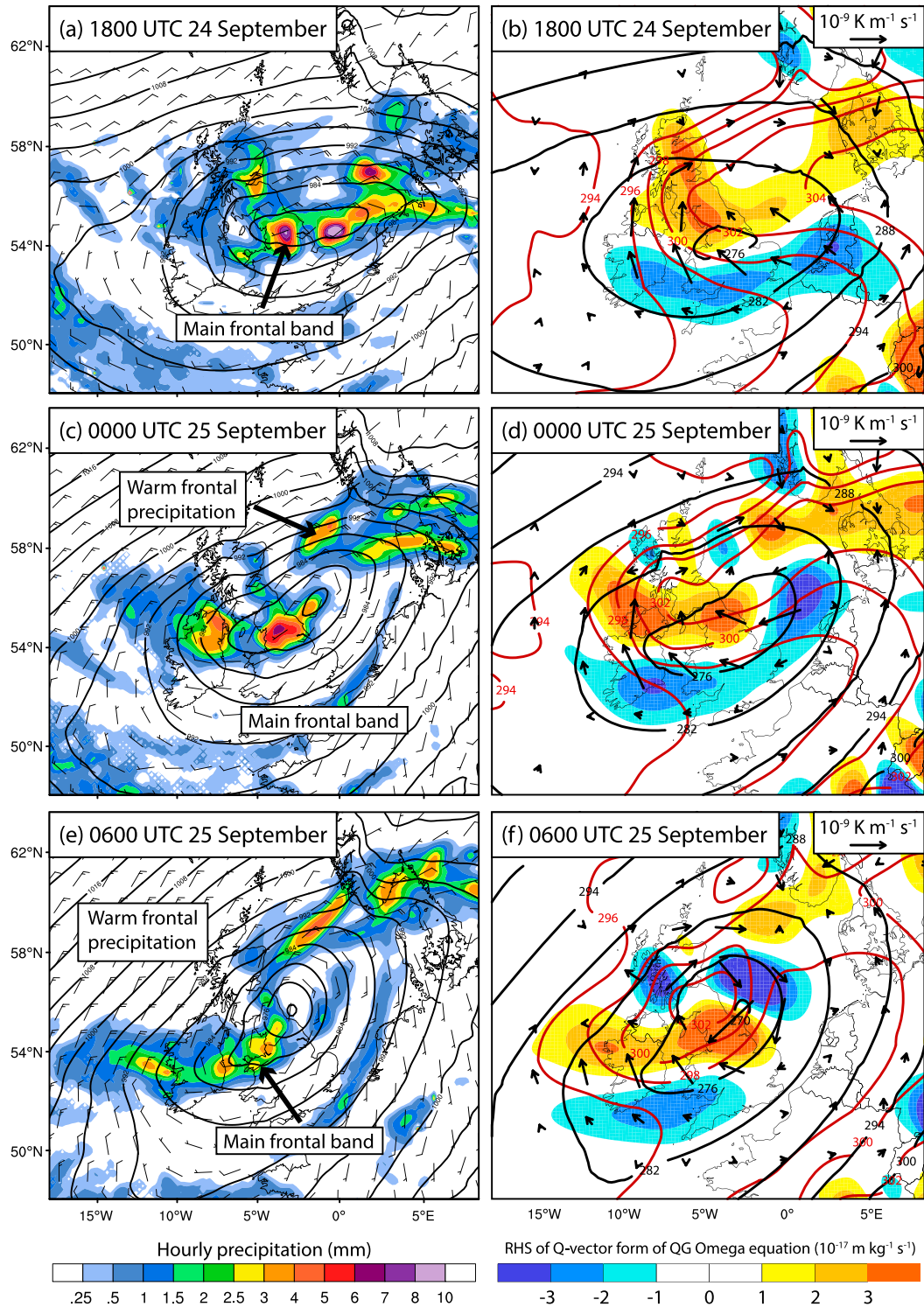
FIG. 11. As in Fig. 10, but for (a),(b) 1800 UTC 24 Sep; (c),(d) 0000 UTC 25 Sep; and (e),(f) 0600 UTC 25 Sep.

et al. 1962; Petterssen and Smebye 1971; Hoskins et al. 1985). In addition, the more amplified pattern in CNTRL, characterized by cyclonic wrap up of the elongated streamer and more prominent ridge building to the

west of the streamer over northern England (cf. Figs. 15c,e and Figs. 15d,f), was likely related to differences in latent heat release between simulations (discussed further in section 6c).
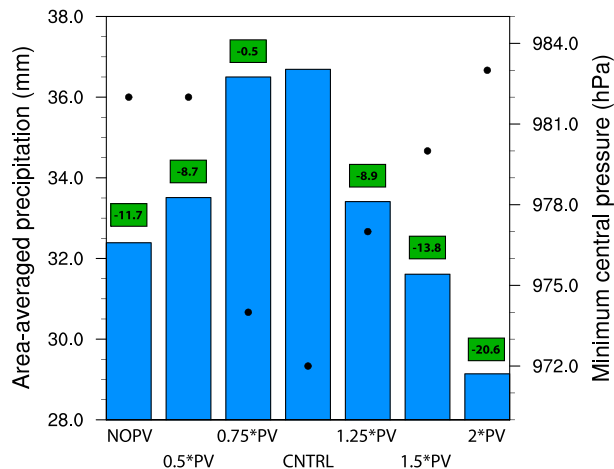
FIG. 12. Area-averaged accumulated precipitation between 1200 UTC 23 Sep and 1200 UTC 26 Sep over the domain in Fig. 9 (blue bars, mm) and minimum cyclone central pressure at the time of maximum cyclone intensity, 0600 UTC 25 Sep (black dots, hPa), for selected WRF simulations. From left to right: PV anomaly removed (NOPV), PV anomaly weakened by 50% (0.5*PV), PV anomaly weakened by 25% (0.75*PV), CNTRL, PV anomaly strengthened by 25% (1.25*PV), PV anomaly strengthened by 50% (1.5*PV), and PV anomaly doubled in strength (2*PV). Atop each bar is the percentage difference in accumulated precipitation between that simulation and CNTRL.
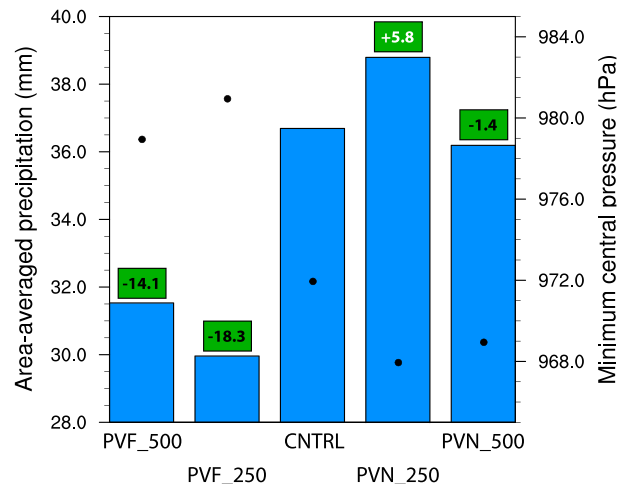
FIG. 13. As in Fig. 12, but for the simulations varying the positioning of the PV anomaly relative to the cyclone. From left to right: PV anomaly moved 500 km farther away from the cyclone (PVF_500), PV anomaly moved 250 km farther away from the cyclone (PVF_250), CNTRL, PV anomaly moved 250 km closer to the cyclone (PVN_250), and PV anomaly moved 500 km closer to the cyclone (PVN_500).

Perturbing the initial position of the PV anomaly also resulted in a bifurcation in the upper-level PV evolution, with a compact trough and weaker surface cyclone developing when the anomaly was moved 250 km farther from the cyclone (Figs. 16a,b) and an elongating streamer wrapping around the deeper cyclone and producing higher rainfall totals when the anomaly was moved 250 km nearer (Figs. 16c,d). Moving the anomaly farther from the cyclone increased the separation distance between the two. This separation was particularly noticeable relative to that in PVN_250 (cf. Figs. 16a and 16c) and meant that at 1200 UTC 24 September, the induced ascent ahead of the PV anomaly was too far from the cyclone to enhance precipitation along the frontal band (not shown). The response of the cyclone to moving the anomaly closer to it at initialization was much smaller than that which occurred when the anomaly was moved farther away (Fig. 13). This differing response, and the differences in upper-level PV between PVN_250 and PVF_250 (cf. Figs. 16a and 16c), suggest that there existed a critical distance beyond which the induced fields of the approaching PV anomaly did not impact the cyclone and its associated rainfall patterns.

b. Differences in QG forcing and precipitation

In 1.5*PV, the strengthened anomaly and associated dipole of 700-hPa QG forcing for vertical motion moved quickly northward between 1200 UTC 24 September and 0000 UTC 25 September, with the frontal rainband fragmenting over northern England in a region of QG forcing for descent ($\leq 3 \times 10^{-17}$ m kg^{-1} s^{-1}) behind the anomaly (Figs. 17a,b and 18a,b). In contrast, a band of moderate rain (5 mm h^{-1}) moved slowly through central and northern England in CNTRL ahead of the elongating PV streamer and associated 700-hPa QG forcing for ascent (Figs. 17c,d and 18c,d). Differences between 0.5*PV and CNTRL became apparent as the rainband strengthened in CNTRL between 1200 UTC 24 September and 0000 UTC 25 September. The cyclone took a similar track in 0.5*PV (cf. Figs. 17c and 17e), but consistent with the weaker upper-level anomaly, QG forcing for vertical motion was smaller (cf. Figs. 17d,f and Figs. 18d,f), the 700-hPa trough was shallower (cf. Figs. 18d and 18f), and rainfall rates were much lower (generally <2 mm h^{-1} in 0.5*PV compared with 5 mm h^{-1} in CNTRL; cf. Figs. 18c and 18e). Stronger lower-tropospheric moisture flux, mainly associated with stronger easterly flow poleward of the lower-tropospheric geopotential height trough, likely also contributed somewhat to the higher rainfall rates in CNTRL relative to 0.5*PV (not shown). However, because the heaviest rain along the frontal band mostly fell to the south of the low center, in westerly rather than easterly flow, we hypothesize that the impact of moist, onshore easterly flow on the rainfall rates within the band was secondary to that of the stronger upper-level QG forcing associated with the PV anomaly.
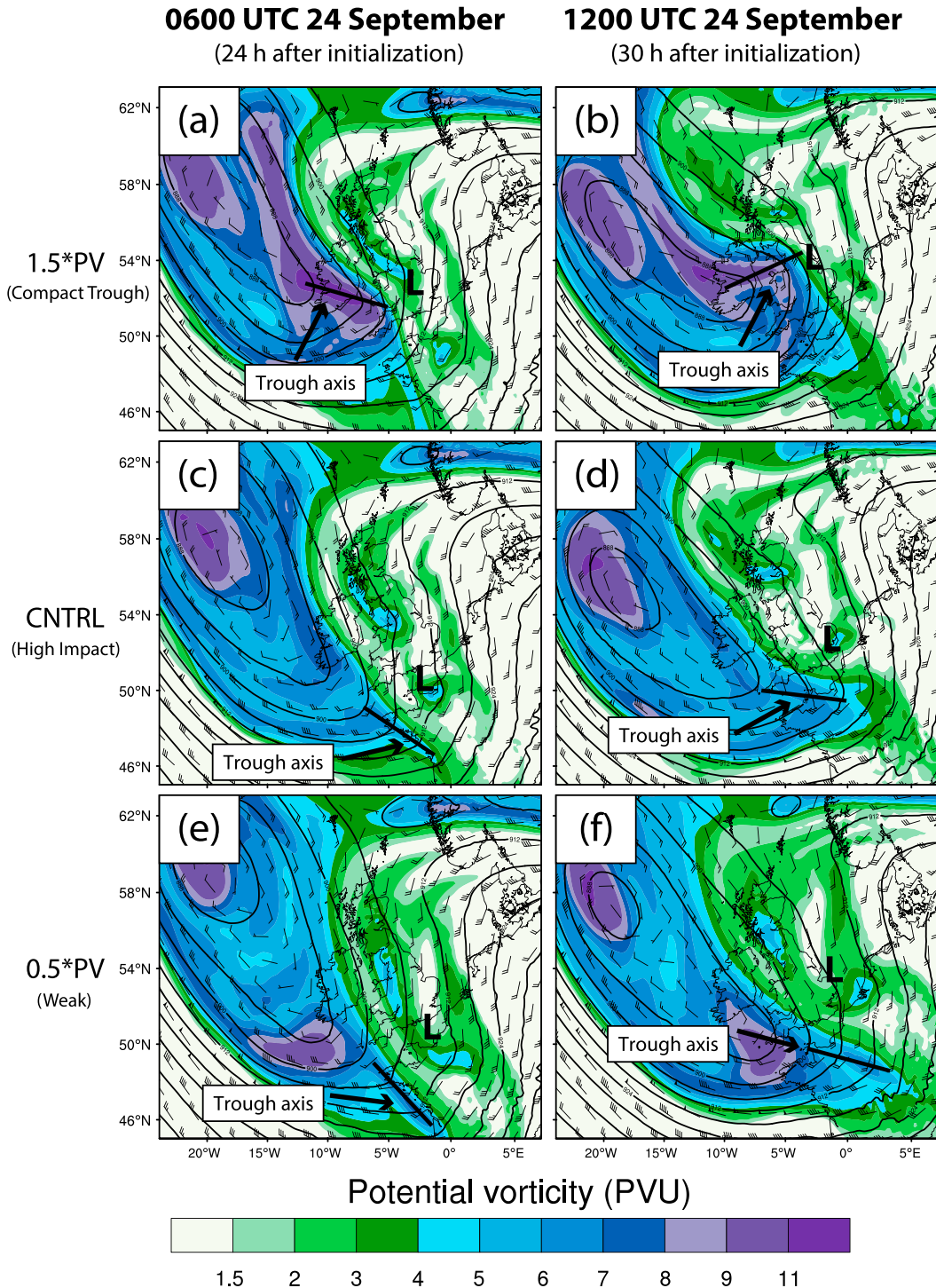
0600 UTC 24 September
(24 h after initialization)

1200 UTC 24 September
(30 h after initialization)

FIG. 14. PV (shaded, PVU) and winds (half-barb represents $2.5\,\mathrm{m\,s^{-1}}$; full barb represents $5\,\mathrm{m\,s^{-1}}$; pennant represents $25\,\mathrm{m\,s^{-1}}$) on the 325-K isentropic surface and 300-hPa geopotential height (black contours, dam). Overlaid is the position of the surface cyclone (L). Results are for (a),(b) 1.5*PV; (c),(d) CNTRL; and (e),(f) 0.5*PV, valid at (left) 0600 UTC 24 Sep and (right) 1200 UTC 24 Sep.

1800 UTC 24 September
(36 h after initialization)

0000 UTC 25 September
(42 h after initialization)
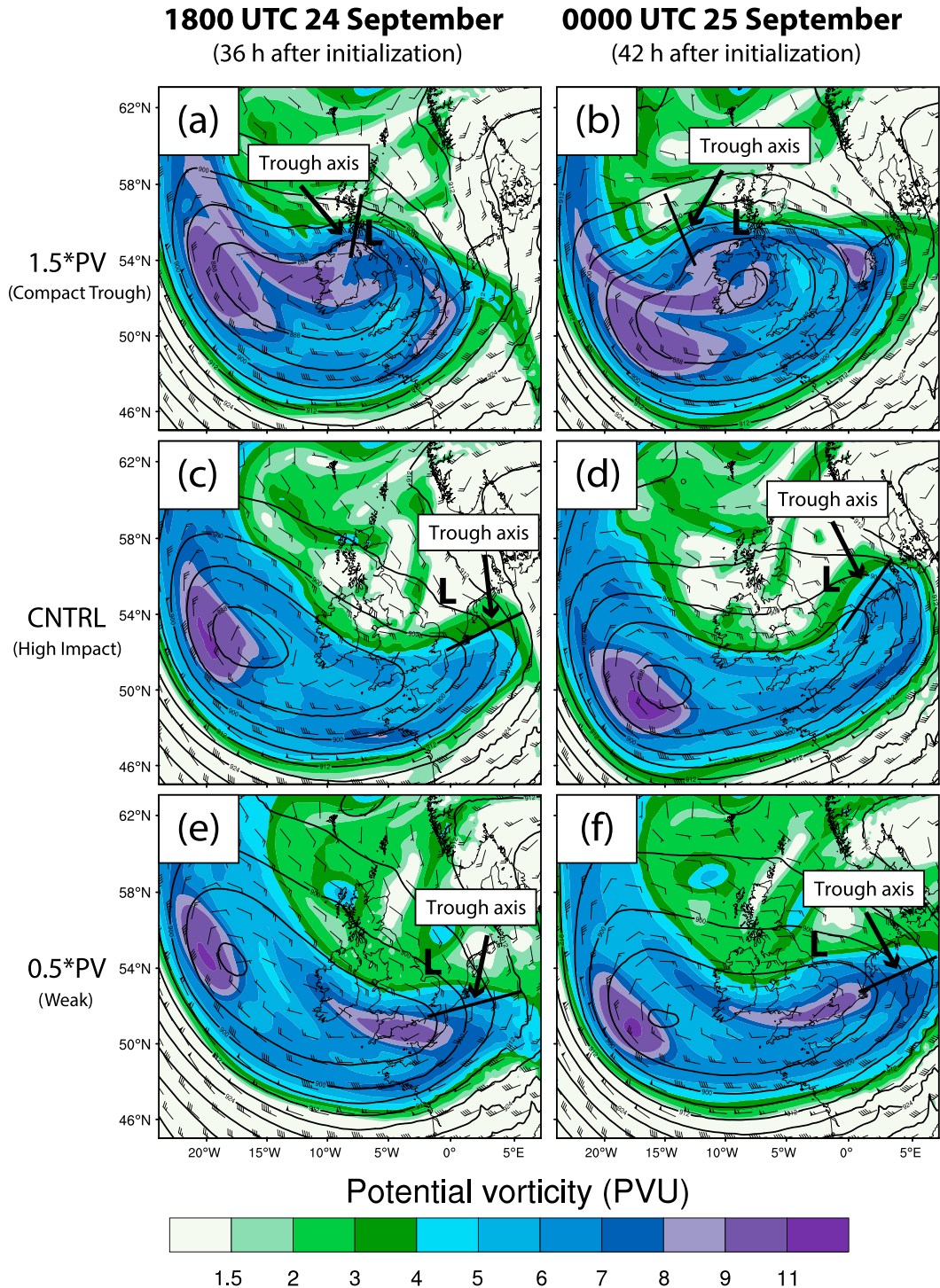
FIG. 15. As in Fig. 14, but for (a),(c),(e) 1800 UTC 24 Sep and (b),(d),(f) 0000 UTC 25 Sep.

c. Behavior of PV anomalies and PV thinking

The relationship between the strength and position of the PV anomaly, and rainfall duration and intensity, in all simulations is illustrated in Fig. 19. The high-impact

rainfall events (CNTRL, 0.75*PV, PVN_250, and PVN_500) are by some distance the longest lasting (Fig. 19), suggesting that the duration rather than the intensity of the rainfall was key to producing a strong flooding event. Our results demonstrate that changes in
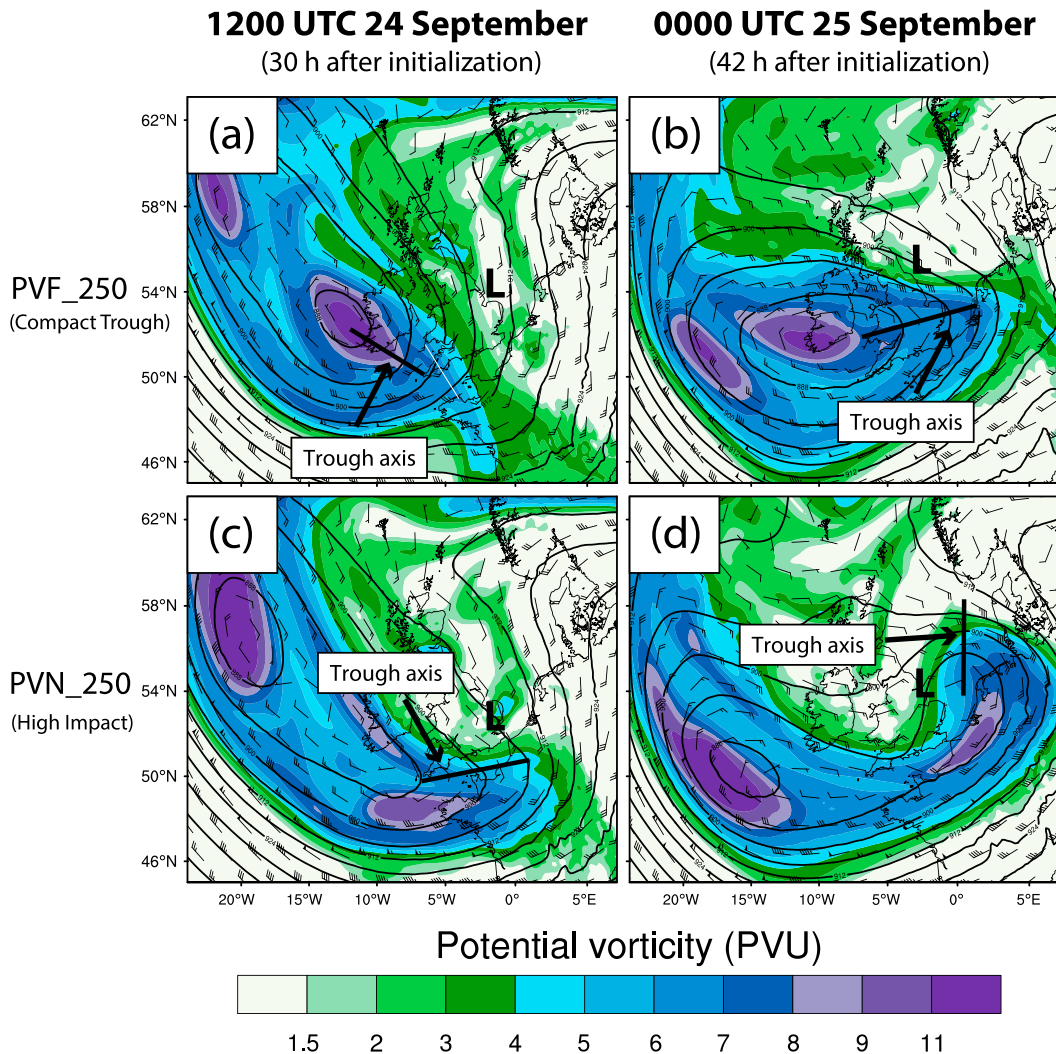
FIG. 16. As in Fig. 14, but for (a),(b) PVF_250 and (c),(d) PVN_250, valid at (left) 1200 UTC 24 Sep and (right) 0000 UTC 25 Sep.

upper-level forcing that increased the speed of the frontal band had a counterintuitive effect on both the total accumulated rainfall (Figs. 12 and 13) and the intensity of the cyclone (Fig. 19). Moreover, the sharp transition between the verifying scenario that produced flooding and the compact-trough scenario characterized by a poleward-shifted and strongly reduced precipitation maximum suggests that the anomaly in the verifying analysis was close to a critical strength. Below this critical strength, the anomaly elongated into a streamer and wrapped around the deepening cyclone (Figs. 14c,d and 15c,d), whereas above this strength, the anomaly remained compact and rotated cyclonically around the large-scale trough over Iceland (Figs. 14a,b and 15a,b). These results corroborate previous idealized studies, which

discovered that interacting anomalies are highly sensitive to small changes in the background flow (e.g., Hakim et al. 1996; Liu and Roebber 2008).

The bifurcation in the evolution of upper-level PV into two solutions, characterized by an eastward-elongating PV streamer and a compact PV anomaly moving poleward, respectively, can be understood in terms of the behavior of vorticity filaments in the presence of background deformation. Idealized studies by Juckes and McIntyre (1987), Dritschel et al. (1991), and Dritschel and Polvani (1992) showed that increasing the strength of a vorticity filament, for a given value of background deformation, encouraged the filament to roll up into a coherent vortex, whereas decreasing the filament's vorticity instead encouraged elongation. Appenzeller et al. (1996) subsequently demonstrated
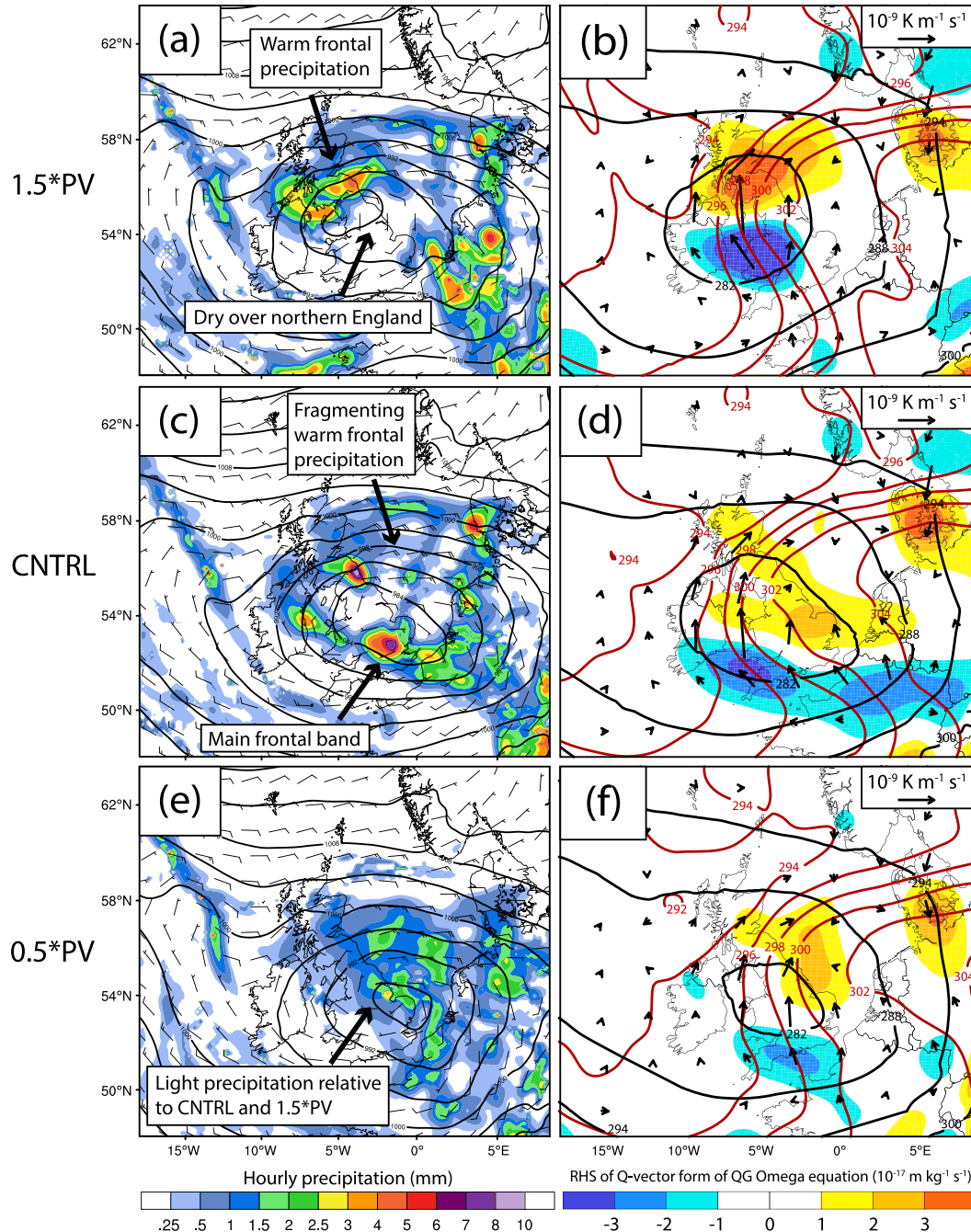
1200 UTC 24 September
(30 h after initialization)

FIG. 17. (a),(c),(e) Hourly accumulated precipitation (shaded, mm), 10-m winds (half-barb represents 2.5 m s^{-1}, full barb represents 5 m s^{-1}, pennant represents 25 m s^{-1}), and mean sea level pressure (black contours, hPa). (b),(d),(f) Right-hand side of the **Q**-vector form of the QG omega equation (shaded, 10^{-17} m kg^{-1} s^{-1}), with warm colors denoting forcing for ascent and cold colors denoting forcing for descent, **Q** vectors (arrows in 10^{-9} K m^{-1} s^{-1}), geopotential height (black contours, dam), and potential temperature (red contours, K) at 700 hPa. Results are for (a),(b) 1.5*PV; (c),(d) CNTRL; and (e),(f) 0.5*PV, valid at 1200 UTC 24 Sep.

0000 UTC 25 September
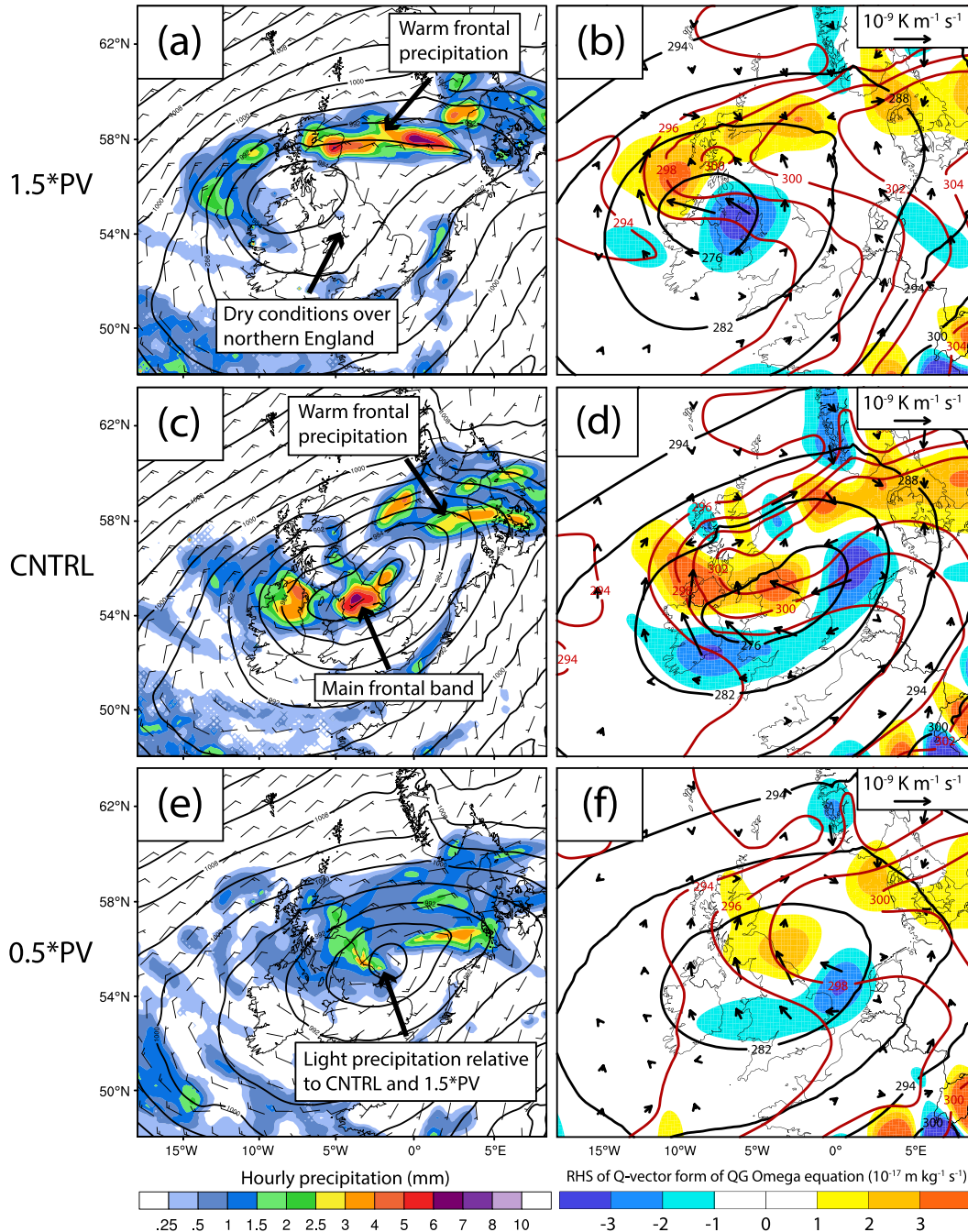## (42 h after initialization)

FIG. 18. As in Fig. 17, but at 0000 UTC 25 Sep.

the applicability of these theoretical ideas to the observed structural variability of stratospheric PV streamers, presenting observational evidence to suggest that as the vorticity of the streamer increases relative to the background deformation, the streamer is increasingly likely to compact and roll up. The tendency of the strengthened anomaly to remain compact rather than elongating to form a PV streamer, as in the verifying
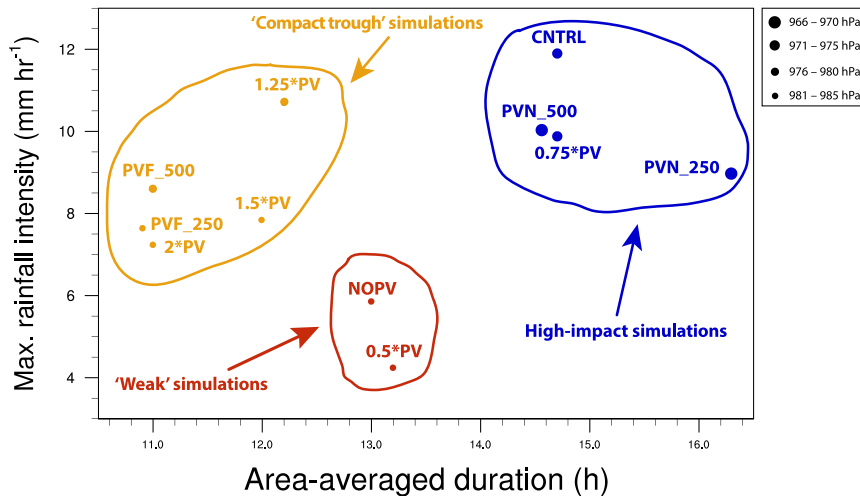
FIG. 19. Relationship between event duration (*x* axis, h) and rainfall intensity (*y* axis, mm h^{-1}) in determining accumulated rainfall for all simulations in Table 1. Rainfall intensity is measured by the maximum rainfall rate within the frontal band as it moves over the United Kingdom between 1800 UTC 23 Sep and 1200 UTC 26 September, thus excluding heavy rainfall over France and the North Sea, and heavy rainfall not associated with the band. Event duration is given by the area-averaged rainfall with an intensity $\geq$1 mm h^{-1} over the domain shown in Fig. 7d, between 1200 UTC 23 Sep and 1200 UTC 26 Sep. Minimum central pressure is size binned according to the legend, and the simulations are grouped into three main scenarios (see text for more details).

analysis, suggests that the mechanism discussed by Dritschel et al. (1991) could be driving the evolution of the PV anomaly in these simulations and subsequently determining the impact of the flooding event across the United Kingdom.

There may be cases where simple, linear thinking holds, but in this and previous studies of extratropical cyclogenesis that used PV surgery to modify initial conditions (e.g., Huo et al. 1999b; Roebber et al. 2002), unexpected results have occurred. This behavior may be a function of several processes. On the synoptic scale, interacting anomalies exhibit strong sensitivity to small changes in the background flow (e.g., Hakim et al. 1996; Liu and Roebber 2008), and furthermore, anomaly evolution is sensitively dependent on the balance between anomaly strength and the large-scale background flow (e.g., Juckes and McIntyre 1987; Dritschel et al. 1991; Dritschel and Polvani 1992; Browning 1993; Appenzeller et al. 1996). In addition, continual diabatic PV modification by latent heat release associated with clouds and precipitation within the cyclone likely amplifies any small initial perturbations applied using PV surgery. The reduction in upper-level PV by latent heat release is a common feature of mature extratropical cyclones (e.g., Davis et al. 1993; Chagnon and Gray 2015; Martínez-Alvarado et al. 2016). In particular, low-PV outflow above regions of latent heat release can enhance downstream ridge building (e.g., Davis et al.

1993; Bosart and Lackmann 1995; Dickinson et al. 1997; Grams et al. 2011) and contribute to the amplification and cyclonic wrap up of upper-level PV anomalies (e.g., Posselt and Martin 2004; Grams et al. 2014; Hardy et al. 2017).

In this case study, persistent latent heat release along the slow-moving rainband in CNTRL contributed to ridge building to the west of the deepening trough and the associated cyclonic wrap up of the trough between 1800 UTC 24 September and 0000 UTC 25 September (see expanding region of <1.5 PVU air on 325 K in Figs. 15c,d). Conversely, the rainfall in 0.5*PV was much lighter and patchier (cf. Figs. 17c,e and Figs. 18c,e), with a more zonally oriented PV evolution and less pronounced ridge building over northern England during the same period, with 325-K PV values mostly >2 PVU (cf. Figs. 15c,e and Figs. 15d,f). The combination of the above factors suggests that PV surgery studies investigating extratropical cyclogenesis, particularly those cases that involve multiple interacting anomalies and strong latent heat release, are likely to often produce surprising results.

7. Conclusions

This study used WRF simulations, with initial conditions modified using PV surgery, and QG omega equation diagnostics to demonstrate the relationship

between the accumulated rainfall in the 23–26 September 2012 U.K. floods and the strength of the upper-level forcing associated with an approaching PV anomaly. In the control simulation and in observations, the cyclone deepened on 24–25 September as the upper-level PV anomaly approached from the west, elongated into a PV streamer, and wrapped around the cyclone. As the cyclone deepened ahead of this PV streamer (20 hPa in 36 h), a band of moderate rain (5 mm h^{-1}) developed to the northwest of the low center in a region of **Q**-vector convergence and associated forcing for ascent ahead of the 700-hPa trough axis and slowly pivoted as the cyclone moved cyclonically through the English Channel and into the North Sea. Latent heat release along the slow-moving rainfall band reduced upper-level PV ahead of the trough in CNTRL, contributing to ridge building and the associated cyclonic wrap up of the trough. Ridge building and the cyclonic wrap up of the trough were strongly reduced in simulations with weaker and less persistent latent heat release, suggesting that latent heat release and associated upper-level PV modification amplified the initial perturbations that were applied using PV surgery.

Somewhat counterintuitively, strengthening the upper-level PV anomaly produced a shallower cyclone (by up to 11 hPa) that moved more quickly through northern England and then westward, resulting in a reduction in accumulated rainfall of up to 21% and in the main region of precipitation being displaced northward into Scotland. Rather than a persistent frontal rainband associated with QG forcing for ascent ahead of the slowly pivoting PV anomaly, the frontal band moved quickly northward across the United Kingdom, with the largest accumulations over eastern Scotland rather than northeast England. This evolution occurred as the strengthened anomaly rotated around a second, larger PV anomaly and associated trough over Iceland rather than moving eastward across the United Kingdom to interact with the cyclone.

The results indicate that errors in the forecast strength of PV anomalies in the upper troposphere and lower stratosphere may lead to dramatic downstream forecast busts when the strength of the anomaly is close to the threshold for elongation versus roll up, and the evolution of the anomaly is thus particularly sensitive to small changes in anomaly strength. The bifurcation in the forecast solution in this study (elongation vs roll up) provides a useful example of how small changes in PV anomaly strength can dramatically shift the upper-level PV evolution and profoundly alter the severity of downstream high-impact weather events in counterintuitive ways.

Two conclusions can be drawn from the sharp transition between the verifying solution (CNTRL) that produced a high-impact flooding event and the solution (1.25*PV) that produced much lower accumulated rainfall (9% lower than CNTRL). First, there was a critical anomaly strength, below which the anomaly moved eastward around the southern flank of the large-scale trough over Iceland and above which the anomaly rotated cyclonically around the trough and moved northward; the 25% increase in anomaly strength in 1.25*PV led to this radically different evolution. Second, the anomaly in the verifying solution was close to this critical strength. These results further demonstrate that stronger upper-level forcing would not have led to a more extreme rainfall event in this case, despite the importance of the approaching PV streamer to the rainfall accumulations across the United Kingdom in the verifying analysis. Although the discovery of optimality is perhaps not surprising for such a high-impact event, this study confirmed that the verifying analysis did indeed represent almost the highest-impact scenario possible for the flooding event, after accounting for sensitivity to the initial position and strength of the PV anomaly.

REFERENCES

Agustí-Panareda, A., C. D. Thorncroft, G. C. Craig, and S. L. Gray, 2004: The extratropical transition of Hurricane Irene (1999): A potential-vorticity perspective. *Quart. J. Roy. Meteor. Soc.*, **130**, 1047–1074, doi:10.1256/qj.02.140.

Ahmadi-Givi, F., G. C. Craig, and R. S. Plant, 2004: The dynamics of a midlatitude cyclone with very strong latent heat release. *Quart. J. Roy. Meteor. Soc.*, **130**, 295–323, doi:10.1256/qj.02.226.

Appenzeller, C., H. C. Davies, and W. A. Norton, 1996: Fragmentation of stratospheric intrusions. *J. Geophys. Res.*, **101**, 1435–1456, doi:10.1029/95JD02674.

Battalio, M., and J. Dyer, 2017: The minimum length scale for evaluating QG omega using high-resolution model data. *Mon. Wea. Rev.*, **145**, 1659–1678, doi:10.1175/MWR-D-16-0241.1.

Bluestein, H. B., 1992: *Principles of Kinematics and Dynamics.* Vol. 1, *Synoptic-Dynamic Meteorology in Midlatitudes*, Oxford University Press, 431 pp.

Boettcher, M., and H. Wernli, 2011: Life cycle study of a diabatic Rossby wave as a precursor to rapid cyclogenesis in the North Atlantic—Dynamics and forecast performance. *Mon. Wea. Rev.*, **139**, 1861–1878, doi:10.1175/2011MWR3504.1.

Bosart, L. F., and G. M. Lackmann, 1995: Postlandfall tropical cyclone reintensification in a weakly baroclinic environment: A case study of Hurricane David (September 1979). *Mon. Wea. Rev.*, **123**, 3268–3291, doi:10.1175/1520-0493(1995)123<3268:PTCRIA>2.0.CO;2.

Bracegirdle, T. J., and S. L. Gray, 2009: The dynamics of a polar low assessed using potential vorticity inversion. *Quart. J. Roy. Meteor. Soc.*, **135**, 880–893, doi:10.1002/qj.411.

Brennan, M. J., G. M. Lackmann, and K. M. Mahoney, 2008: Potential vorticity (PV) thinking in operations: The utility of nonconservation. *Wea. Forecasting*, **23**, 168–182, doi:10.1175/2007WAF2006044.1.

Browning, K. A., 1993: Evolution of a mesoscale upper tropospheric vorticity maximum and comma cloud from a cloud-free two-dimensional potential vorticity anomaly. *Quart. J. Roy. Meteor. Soc.*, **119**, 883–906, doi:10.1002/qj.49711951302.

Catto, J. L., and S. Pfahl, 2013: The importance of fronts for extreme precipitation. *J. Geophys. Res. Atmos.*, **118**, 10 791–10 801, doi:10.1002/jgrd.50852.

Chagnon, J. M., and S. L. Gray, 2015: A diabatically generated potential vorticity structure near the extratropical tropopause in three simulated extratropical cyclones. *Mon. Wea. Rev.*, **143**, 2337–2347, doi:10.1175/MWR-D-14-00092.1.

Champion, A. J., R. P. Allan, and D. A. Lavers, 2015: Atmospheric rivers do not explain UK summer extreme rainfall. *J. Geophys. Res. Atmos.*, **120**, 6731–6741, doi:10.1002/2014JD022863.

Charney, J. G., 1947: The dynamics of long waves in a baroclinic westerly current. *J. Meteor.*, **4**, 135–162, doi:10.1175/1520-0469(1947)004<0136:TDOLWI>2.0.CO;2.

——, 1955: The use of the primitive equations of motion in numerical prediction. *Tellus*, **7**, 22–26, doi:10.3402/tellusa.v7i1.8772.

Davis, C. A., 1992: A potential-vorticity diagnosis of the importance of initial structure and condensational heating in observed extratropical cyclogenesis. *Mon. Wea. Rev.*, **120**, 2409–2428, doi:10.1175/1520-0493(1992)120<2409:APVDOT>2.0.CO;2.

——, and K. A. Emanuel, 1991: Potential vorticity diagnostics of cyclogenesis. *Mon. Wea. Rev.*, **119**, 1929–1953, doi:10.1175/1520-0493(1991)119<1929:PVDOC>2.0.CO;2.

——, M. T. Stoelinga, and Y.-H. Kuo, 1993: The integrated effect of condensation in numerical simulations of extratropical cyclogenesis. *Mon. Wea. Rev.*, **121**, 2309–2330, doi:10.1175/1520-0493(1993)121<2309:TIEOCI>2.0.CO;2.

Dickinson, M. J., L. F. Bosart, W. E. Bracken, G. J. Hakim, D. M. Schultz, M. A. Bedrick, and K. R. Tyle, 1997: The March 1993 superstorm cyclogenesis: Incipient phase synoptic- and convective-scale flow interaction and model performance. *Mon. Wea. Rev.*, **125**, 3041–3072, doi:10.1175/1520-0493(1997)125<3041:TMSCIP>2.0.CO;2.

Dritschel, D. G., and L. M. Polvani, 1992: The roll-up of vorticity strips on the surface of a sphere. *J. Fluid Mech.*, **234**, 47–69, doi:10.1017/S0022112092000697.

——, P. H. Haynes, M. N. Juckes, and T. G. Shepherd, 1991: The stability of a two-dimensional vorticity filament under uniform strain. *J. Fluid Mech.*, **230**, 647–665, doi:10.1017/S0022112091000915.

Eady, E. T., 1949: Long waves and cyclone waves. *Tellus*, **1** (3), 33–52, doi:10.3402/tellusa.v1i3.8507.

Ertel, H., 1942: Ein neuer hydrodynamischer wirbelsatz. *Meteor. Z.*, **59**, 271–281.

Fehlmann, R., C. Quadri, and H. C. Davies, 2000: An Alpine rainstorm: Sensitivity to the mesoscale upper-level structure. *Wea. Forecasting*, **15**, 4–28, doi:10.1175/1520-0434(2000)015<0004:AARSTT>2.0.CO;2.

Gaza, R. S., and L. F. Bosart, 1990: Trough-merger characteristics over North America. *Wea. Forecasting*, **5**, 314–331, doi:10.1175/1520-0434(1990)005<0314:TMCONA>2.0.CO;2.

Grams, C. M., and Coauthors, 2011: The key role of diabatic processes in modifying the upper-tropospheric wave guide: A North Atlantic case study. *Quart. J. Roy. Meteor. Soc.*, **137**, 2174–2193, doi:10.1002/qj.891.

——, S. C. Jones, and C. A. Davis, 2013: The impact of Typhoon Jangmi (2008) on the midlatitude flow. Part II: Downstream evolution. *Quart. J. Roy. Meteor. Soc.*, **139**, 2165–2180, doi:10.1002/qj.2119.

——, H. Binder, S. Pfahl, N. Piaget, and H. Wernli, 2014: Atmospheric processes triggering the central European floods in June 2013. *Nat. Hazards Earth Syst. Sci.*, **14**, 1691–1702, doi:10.5194/nhess-14-1691-2014.

Hakim, G. J., D. Keyser, and L. F. Bosart, 1996: The Ohio valley wave-merger cyclogenesis event of 25–26 January 1978. Part II: Diagnosis using quasigeostrophic potential vorticity inversion. *Mon. Wea. Rev.*, **124**, 2176–2205, doi:10.1175/1520-0493(1996)124<2176:TOVWMC>2.0.CO;2.

Hand, W. H., N. I. Fox, and C. G. Collier, 2004: A study of twentieth-century extreme rainfall events in the United Kingdom with implications for forecasting. *Meteor. Appl.*, **11**, 15–31, doi:10.1017/S1350482703001117.

Hardy, S., D. M. Schultz, and G. Vaughan, 2017: Early evolution of the 23–26 September 2012 U.K. floods: Tropical Storm Nadine and diabatic heating due to cloud microphysics. *Mon. Wea. Rev.*, **145**, 543–563, doi:10.1175/MWR-D-16-0200.1.

Hong, S.-Y., Y. Noh, and J. Dudhia, 2006: A new vertical diffusion package with an explicit treatment of entrainment processes. *Mon. Wea. Rev.*, **134**, 2318–2341, doi:10.1175/MWR3199.1.

Hoskins, B. J., and M. A. Pedder, 1980: The diagnosis of middle latitude synoptic development. *Quart. J. Roy. Meteor. Soc.*, **106**, 707–719, doi:10.1002/qj.49710645004.

——, I. Draghici, and H. C. Davies, 1978: A new look at the ω-equation. *Quart. J. Roy. Meteor. Soc.*, **104**, 31–38, doi:10.1002/qj.49710443903.

——, M. E. McIntyre, and A. W. Robertson, 1985: On the use and significance of isentropic potential vorticity maps. *Quart. J. Roy. Meteor. Soc.*, **111**, 877–946, doi:10.1002/qj.49711147002.

Huo, Z., D.-L. Zhang, and J. R. Gyakum, 1999a: Interaction of potential vorticity anomalies in extratropical cyclogenesis. Part I: Static piecewise inversion. *Mon. Wea. Rev.*, **127**, 2546–2561, doi:10.1175/1520-0493(1999)127<2546:IOPVAI>2.0.CO;2.

——, ——, and ——, 1999b: Interaction of potential vorticity anomalies in extratropical cyclogenesis. Part II: Sensitivity to

initial perturbations. *Mon. Wea. Rev.*, **127**, 2563–2575, doi:10.1175/1520-0493(1999)127<2563:IOPVAI>2.0.CO;2.

Iacono, M. J., J. S. Delamere, E. J. Mlawer, M. W. Shephard, S. A. Clough, and W. D. Collins, 2008: Radiative forcing by long-lived greenhouse gases: Calculations with the AER radiative transfer models. *J. Geophys. Res.*, **113**, D13103, doi:10.1029/2008JD009944.

Juckes, M. N., and M. E. McIntyre, 1987: A high-resolution one-layer model of breaking planetary waves in the stratosphere. *Nature*, **328**, 590–596, doi:10.1038/328590a0.

Kain, J. S., 2004: The Kain–Fritsch convective parameterization: An update. *J. Appl. Meteor.*, **43**, 170–181, doi:10.1175/1520-0450(2004)043<0170:TKCPAU>2.0.CO;2.

——, and J. M. Fritsch, 1990: A one-dimensional entraining/detraining plume model and its application in convective parameterization. *J. Atmos. Sci.*, **47**, 2784–2802, doi:10.1175/1520-0469(1990)047<2784:AODEPM>2.0.CO;2.

——, and ——, 1993: Convective parameterization for mesoscale models: The Kain–Fritsch scheme. *The Representation of Cumulus Convection in Numerical Models*, *Meteor. Monogr.*, No. 24, Amer. Meteor. Soc., 165–170.

Klein, P. M., P. A. Harr, and R. L. Elsberry, 2002: Extratropical transition of western North Pacific tropical cyclones: Midlatitude and tropical cyclone contributions to re-intensification. *Mon. Wea. Rev.*, **130**, 2240–2259, doi:10.1175/1520-0493(2002)130<2240:ETOWNP>2.0.CO;2.

Lavers, D. A., R. P. Allan, E. F. Wood, G. Villarini, D. J. Brayshaw, and A. J. Wade, 2011: Winter floods in Britain are connected to atmospheric rivers. *Geophys. Res. Lett.*, **38**, L23803, doi:10.1029/2011GL049783.

——, G. Villarini, R. P. Allan, E. F. Wood, and A. J. Wade, 2012: The detection of atmospheric rivers in atmospheric reanalyses and their links to British winter floods and the large-scale climatic circulation. *J. Geophys. Res.*, **117**, D20106, doi:10.1029/2012JD018027.

Liu, Z., and P. J. Roebber, 2008: Vortex-driven sensitivity in deformation flow. *J. Atmos. Sci.*, **65**, 3819–3839, doi:10.1175/2008JAS2745.1.

Mark, A., 2013: Diving into flood risk. Risk Management Solutions, http://www.rms.com/blog/2013/07/30/diving-into-flood-risk/.

Martínez-Alvarado, O., S. L. Gray, and J. Methven, 2016: Diabatic processes and the evolution of two contrasting summer extratropical cyclones. *Mon. Wea. Rev.*, **144**, 3251–3276, doi:10.1175/MWR-D-15-0395.1.

McTaggart-Cowan, R., J. R. Gyakum, and M. K. Yau, 2001: Sensitivity testing of extratropical transitions using potential vorticity inversions to modify initial conditions: Hurricane Earl case study. *Mon. Wea. Rev.*, **129**, 1617–1636, doi:10.1175/1520-0493(2001)129<1617:STOETU>2.0.CO;2.

——, ——, and ——, 2004: The impact of tropical remnants on extratropical cyclogenesis: Case study of Hurricanes Danielle and Earl (1998). *Mon. Wea. Rev.*, **132**, 1933–1951, doi:10.1175/1520-0493(2004)132<1933:TIOTRO>2.0.CO;2.

Met Office, 2009: Weather radar. National Meteorological Library and Archive Fact Sheet 15, 22 pp., http://www.metoffice.gov.uk/binaries/content/assets/mohippo/pdf/j/h/fact_sheet_no._15.pdf.

Met Office Press Office, 2012: Storm caused by most intense low to cross UK in September in 30 years. Met Office, http://metofficenews.wordpress.com/2012/09/26/storm-caused-by-most-intense-low-to-cross-uk-in-30-years/.

Monin, A. S., and A. M. Obukhov, 1954: Basic laws of turbulent mixing in the surface layer of the atmosphere (in Russian). *Tr. Geofiz. Inst. Akad. Nauk SSSR*, **24**, 163–187.

Pantillon, F. P., J.-P. Chaboureau, and E. Richard, 2016: Vortex–vortex interaction between Hurricane Nadine (2012) and an Atlantic cutoff dropping the predictability over the Mediterranean. *Quart. J. Roy. Meteor. Soc.*, **142**, 419–432, doi:10.1002/qj.2635.

Parry, S., T. Marsh, and M. Kendon, 2013: 2012: From drought to floods in England and Wales. *Weather*, **68**, 268–273, doi:10.1002/wea.2152.

Petterssen, S., 1936: Contribution to the theory of frontogenesis. *Geophys. Publ.*, **11** (6), 1–27.

——, 1955: A general survey of factors influencing development at sea level. *J. Meteor.*, **12**, 36–42, doi:10.1175/1520-0469(1955)012<0036:AGSOFI>2.0.CO;2.

——, and S. J. Smebye, 1971: On the development of extratropical cyclones. *Quart. J. Roy. Meteor. Soc.*, **97**, 457–482, doi:10.1002/qj.49709741407.

——, D. L. Bradbury, and K. Pedersen, 1962: The Norwegian cyclone model in relation to heat and cold sources. *Geofys. Publ.*, **24**, 243–280.

Pfahl, S., and H. Wernli, 2012: Quantifying the relevance of cyclones for precipitation extremes. *J. Climate*, **25**, 6770–6780, doi:10.1175/JCLI-D-11-00705.1.

Posselt, D. J., and J. E. Martin, 2004: The effect of latent heat release on the evolution of a warm occluded thermal structure. *Mon. Wea. Rev.*, **132**, 578–599, doi:10.1175/1520-0493(2004)132<0578:TEOLHR>2.0.CO;2.

Quinting, J. F., and S. C. Jones, 2016: On the impact of tropical cyclones on Rossby wave packets: A climatological perspective. *Mon. Wea. Rev.*, **144**, 2021–2048, doi:10.1175/MWR-D-14-00298.1.

Reed, R. J., and M. D. Albright, 1986: A case of explosive cyclogenesis in the eastern Pacific. *Mon. Wea. Rev.*, **114**, 2297–2319, doi:10.1175/1520-0493(1986)114<2297:ACSOEC>2.0.CO;2.

——, M. T. Stoelinga, and Y.-H. Kuo, 1992: A model-aided study of the origin and evolution of the anomalously high potential vorticity in the inner region of a rapidly deepening marine cyclone. *Mon. Wea. Rev.*, **120**, 893–913, doi:10.1175/1520-0493(1992)120<0893:AMASOT>2.0.CO;2.

Riemer, M., and S. C. Jones, 2010: The downstream impact of tropical cyclones on a developing baroclinic wave in idealized scenarios of extratropical transition. *Quart. J. Roy. Meteor. Soc.*, **136**, 617–637, doi:10.1002/qj.605.

——, ——, and C. A. Davis, 2008: The impact of extratropical transition on the downstream flow: An idealized modelling study with a straight jet. *Quart. J. Roy. Meteor. Soc.*, **134**, 69–91, doi:10.1002/qj.189.

Ritchie, E., and R. L. Elsberry, 2007: Simulations of the extratropical transition of tropical cyclones: Phasing between the upper-level trough and tropical cyclones. *Mon. Wea. Rev.*, **135**, 862–876, doi:10.1175/MWR3303.1.

Roebber, P. J., D. M. Schultz, and R. Romero, 2002: Synoptic regulation of the 3 May 1999 tornado outbreak. *Wea. Forecasting*, **17**, 399–429, doi:10.1175/1520-0434(2002)017<0399:SROTMT>2.0.CO;2.

Romero, R., 2001: Sensitivity of a heavy-rain-producing western Mediterranean cyclone to embedded potential-vorticity anomalies. *Quart. J. Roy. Meteor. Soc.*, **127**, 2559–2597, doi:10.1002/qj.49712757805.

Rossby, C. G., 1940: Planetary flow patterns in the atmosphere. *Quart. J. Roy. Meteor. Soc.*, **66**, 68–87.

Sanders, F., 1986: Explosive cyclogenesis in the west-central North Atlantic Ocean, 1981–84. Part I: Composite structure and mean behavior. *Mon. Wea. Rev.*, **114**, 1781–1794, doi:10.1175/1520-0493(1986)114<1781:ECITWC>2.0.CO;2.

Skamarock, W. C., and Coauthors, 2008: A description of the Advanced Research WRF version 3. NCAR Tech. Note NCAR/TN-475+STR, 113 pp., doi:10.5065/D68S4MVH.

Stoelinga, M. T., 1996: A potential vorticity-based study of the role of diabatic heating and friction in a numerically simulated baroclinic cyclone. *Mon. Wea. Rev.*, **124**, 849–874, doi:10.1175/1520-0493(1996)124<0849:APVBSO>2.0.CO;2.

Sutcliffe, R. C., 1939: Cyclonic and anticyclonic development. *Quart. J. Roy. Meteor. Soc.*, **65**, 518–524, doi:10.1002/qj.49706528208.

——, 1947: A contribution to the problem of development. *Quart. J. Roy. Meteor. Soc.*, **73**, 370–383, doi:10.1002/qj.49707331710.

——, and A. G. Forsdyke, 1950: The theory and use of upper air thickness patterns in forecasting. *Quart. J. Roy. Meteor. Soc.*, **76**, 189–217, doi:10.1002/qj.49707632809.

Thompson, G., P. R. Field, R. M. Rasmussen, and W. D. Hall, 2008: Explicit forecasts of winter precipitation using an improved bulk microphysics scheme. Part II: Implementation of a new snow parameterization. *Mon. Wea. Rev.*, **136**, 5095–5115, doi:10.1175/2008MWR2387.1.

Uccellini, L. W., 1986: The possible influence of upstream upper-level baroclinic processes on the development of the *QE II* storm. *Mon. Wea. Rev.*, **114**, 1019–1027, doi:10.1175/1520-0493(1986)114<1019:TPIOUU>2.0.CO;2.

——, D. Keyser, K. F. Brill, and C. H. Wash, 1985: The Presidents' Day cyclone of 18–19 February 1979: Influence of upstream trough amplification and associated tropopause folding on rapid cyclogenesis. *Mon. Wea. Rev.*, **113**, 962–988, doi:10.1175/1520-0493(1985)113<0962:TPDCOF>2.0.CO;2.